

ORCA - Online Research @ Cardiff

This is an Open Access document downloaded from ORCA, Cardiff University's institutional repository:https://orca.cardiff.ac.uk/id/eprint/182311/

This is the author's version of a work that was submitted to / accepted for publication.

Citation for final published version:

Furukawa, H., Iwata, S., Phillips, T. N., Lind, S. J. and Walters, M J. 2025. The influence of viscoelasticity on the dynamics of encapsulated microbubbles near a rigid surface forced by ultrasound. Journal of Non-Newtonian Fluid Mechanics, 105518. 10.1016/j.jnnfm.2025.105518

Publishers page: http://dx.doi.org/10.1016/j.jnnfm.2025.105518

Please note:

Changes made as a result of publishing processes such as copy-editing, formatting and page numbers may not be reflected in this version. For the definitive version of this publication, please refer to the published source. You are advised to consult the publisher's version if you wish to cite this paper.

This version is being made available in accordance with publisher policies. See http://orca.cf.ac.uk/policies.html for usage policies. Copyright and moral rights for publications made available in ORCA are retained by the copyright holders.



The Influence of Viscoelasticity on the Dynamics of Encapsulated Microbubbles Near a Rigid Surface Forced by Ultrasound

H. Furukawa^a, S. Iwata^a, T. N. Phillips^{b,*}, S. J. Lind^c, M. J. Walters^b

^aDepartment of Life Science and Applied Chemistry, Nagoya Institute of Technology, Nagoya 466-8555, Japan ^bSchool of Mathematics, Cardiff University, Abacws, Cardiff, CF24 4AG, U.K. ^cSchool of Engineering, Cardiff University, Queen's Buildings, Cardiff, CF24 3AA, U.K.

Abstract

The dynamics of thin-shell encapsulated microbubbles (EMBs) in viscoelastic fluids forced by ultrasound are investigated in this paper. EMBs, which are gas-filled microbubbles encased in a stiff albumin or flexible lipid shell, have been shown to improve the performance of biomedical procedures such as ultrasound contrast imaging and sonoporation. To gain computationally efficient initial insights, the flow is assumed irrotational and axisymmetric, and is solved via the boundary element method. The viscoelastic fluid is modelled using the Oldroyd B model with both the fluid and the properties of the shell accounted for through the dynamic boundary condition at the bubble surface. A large bubble shell thickness is found to have a significant stabilising effect on the bubble, markedly reducing bubble deformation and response to the ultrasound pulse. For realistic ultrasound and biological fluid parameters, shell properties appear to dominate over fluid rheology. Although at lower shell thicknesses the dynamics are governed by a competition between viscous, elastic and inertial forces. A larger response is observed for lower frequency ultrasound and for pressure amplitudes typical to sonoporation, large translational movement in the direction of the pulse is predicted as well as deformation and the potential for bubble fragmentation. The model and quantitative insights herein have the potential to form the basis of a low-cost computational tool useful for EMB design, fabrication and

^{*}Corresponding author. Email: PhillipsTN@cardiff.ac.uk

characterisation in the near future.

1. Introduction

Ultrasound is one of the predominant methods for medical diagnosis since it is safe, fast and inexpensive compared to other techniques. While the image quality using conventional procedures is often unsatisfactory, it can be significantly improved through the introduction of encapsulated microbubbles (EMBs). The interaction of an ultrasound beam with a microbubble causes the bubble to expand and contract since the internal gas is much more compressible than the surrounding tissue. For a typical EMB of the order 1 μ m, this occurs most readily for the resonance frequency lying in the range (2 - 10 MHz), which is the range typically used for ultrasound imaging [1]. Due to this, EMBs return significantly stronger echoes than tissue reflectors of a similar size and it is this property that is responsible for their efficacy as contrast agents.

An EMB, also known as an ultrasound contrast agent (UCA), is typically filled with air or a high-molecular-weight low-solubility gas encased by an albumin or lipid shell. The bubbles are typically $1-10 \mu m$ in diameter [2] which is small enough to pass through capillaries when suspended in blood. The encapsulating shell stabilises the bubble against hydrodynamical forces and consequently an EMB is able to reach almost any desired area of the body without collapsing or dissolving. In recent years, targeted contrast agents have also been developed to selectively adhere to a specific site [3]. EMBs have also been investigated for use in sonoporation [4] and gene therapy [5]. Sonoporation is the use of ultrasound to increase the permeability of cell membranes; ideally creating transient pores which allow the uptake of large molecules such as DNA (a few nm in size) into a cell without destroying it (known as transfection). The molecules can be transferred to the desired site using EMBs, which are then excited using an ultrasound field. The physics behind the increased cell permeability and the transfection of the material are complex, although Miller et al. [5] have shown that cavitation bubbles play a role. Bouakaz and Escoffre [6] provide a recent review on the use of EMBs as a theraputic tool, noting that despite three decades of research, key challenges remain, including standardisation of operating parameters (e.g. ultrasound and microbubble properties) to help deliver effective treatments whilst also maintaining patient safety/minimising tissue damage. It is in this search for optimal parameter guidelines that modelling and numerical simulations can be particularly beneficial.

The majority of previous numerical studies on EMBs have investigated

spherical oscillations, usually involving a modified Rayleigh-Plesset equation with extra terms accounting for the properties of the shell (see, for example, de Jong et al. [7], Church [8], and Hoff [9]). These extra terms can also be constructed to model more advanced physics including buckling and rupture [10], shell viscoelasticity [11], or strain-softening [12] (but all still within the spherical model setting). Whilst some models (such as Church [8] and Hoff [9]) employ a finite shell thickness, the disparate length scales between the microbubble radius and the shell thickness (i.e. micrometres compared to nanometres) have the potential to pose a significant modelling challenge for more general dynamics. This has led to the development of more sophisticated "zero-thickness" interfacial rheological models that may be based on either Newtonian or viscoelastic rheology and characterised by an interfacial viscosity, elasticity and surface tension [13, 14]. Indeed, it can be shown that many previous shell modelling approaches (including those of Church [8], Hoff [9], de Jong et al. [7], and Marmottant et al. [10]) can be reduced to an equivalent interfacial rheological model described by effective interfacial parameters (an effective dilatational viscosity and surface tension, with coefficients potentially dependent on bubble radius) [15].

Generally, the shell has a stabilising effect on the bubble dynamics, but non-spherical behaviour of EMBs can still occur due to the presence of nearby structures or interaction with a strong ultrasound field. For example, Wang et al. [16] used the boundary element method (BEM) to model a non-spherical EMB near a rigid surface that is forced by ultrasound. A modification of Hoff's spherical model [9] was used and applied through the dynamic boundary condition at the bubble surface. The majority of the results presented were for an inviscid fluid although some viscous Newtonian examples were also considered. However, neither biological fluids nor soft tissue behave as Newtonian fluids. Therefore, the challenge in studying the behaviour of EMBs in a biomedical context lies in modelling viscoelastic and compressible behaviour.

In terms of compressibility, numerical simulations for non-spherical bubbles have been largely restricted to inviscid and Newtonian fluids [17, 18, 19]. The simulations for non-spherical bubbles that have been performed for viscoelastic fluids have been largely based on Maxwell-type models in which compressibility is neglected [20, 21]. However, Lind and Phillips [22] considered the non-spherical collapse of a 2-D bubble near a rigid wall in a weakly compressible upper-convected Maxwell fluid and showed that viscoelasticity can prevent the formation of a liquid jet and is therefore likely to mitigate

cavitation damage. More recently, Lang et al. [23] have considered bubble collapse in a compressible viscoelastic fluid, with the 3-D governing equations solved using a finite volume method. However, despite the 3-D capability, the focus remained on spherical dynamics but with the finite volume method able to capture compressible flow dynamics (e.g. shockwaves) in the ambient fluid.

Regarding viscoelasticity, a common feature of viscoelastic bubble dynamics is the oscillation of the bubble surface in time. In the absence of any internal gas content, this effect results from competing inertial and elastic forces and typically occurs in fluids with large elasticities and at low-tomoderate Reynolds numbers. In the spherical case, this effect can be observed by solving the Rayleigh-Plesset equation generalised to accommodate a general extra stress and so a variety of different constitutive relations. For example, Fogler and Goddard [24] conducted one of the first such studies of viscoelastic bubble collapse by using a Rayleigh-Plesset equation, solved via finite differences, to model collapse in a linear Maxwell fluid for a range of Reynolds and Deborah numbers. They noted existence of a criterion at very large Deborah numbers, around which the bubble may oscillate indefinitely about an equilibrium radius or otherwise collapse completely without oscillation. A key finding of the study was that fluid elasticity can inhibit bubble collapse and produce large oscillations in radius if the fluid relaxation time is of the order of the Rayleigh collapse time.

Allen and Roy [25, 26] considered the forced oscillation of a bubble in an infinite expanse of fluid using incompressible linear and nonlinear Maxwell models. They found significant differences between Newtonian and viscoelastic cases. In particular, Allen and Roy [25] showed that there were significant differences between the viscoelastic and Newtonian cases with the addition of elasticity when studying sub-harmonic oscillations. Viscoelasticity modulates the amplitude in a manner corresponding to the relaxation time of the fluid. Allen and Roy [26] extended the analysis to study the oscillation of bubbles in nonlinear viscoelastic media. Agreement with the predictions of linear viscoelasticity was found for small deformations. However, it was also found that beyond the limit of small deformations, elasticity can increase the generation of secondary harmonics and serve to increase the maximum bubble radius. Since cavitation damage has been linked to large bubble expansions, this is an important discovery in the context of bubble dynamics in biological fluids and tissue.

Khismatullin and Nadim [27] performed a theoretical investigation of the

small-amplitude oscillations of a microbubble encapsulated by a viscoelastic shell and immersed in a slightly compressible viscoelastic fluid. The viscoelastic properties of the shell and the liquid were modelled using the Kelvin-Voigt and 4-constant Oldroyd models, respectively. The method of matched asymptotic expansions is used to derive an equation for the radial oscillation of the bubble. They showed that the resonance frequency for the EMB is highly dependent on viscous damping and therefore, significantly differs from the undamped natural frequency. The effects of the shell and liquid parameters on the resonance frequency and scattering cross sections are analyzed.

Yang and Church [28] investigated the large-amplitude oscillations of cavitation bubbles driven by an ultrasonic field using the Keller-Miksis equation in conjunction with a Kelvin-Voigt model to describe viscoelasticity. They found that elasticity increases the inertial cavitation threshold, and subharmonic signals may only be detectable in certain ranges of radius and pressure amplitude.

Brujan [29, 30] investigated spherical bubble dynamics in a compressible viscoelastic liquid using a linear Oldroyd model and a simplified singular-perturbation method to first-order in the bubble-wall Mach number. He showed that, under conditions comparable to those existing during cavitation, the effect of fluid rheology on bubble dynamics is negligible for values of the Reynolds number beyond a critical value while the only significant influence is that of liquid compressibility. For larger values of the Reynolds number sound emission was found to be the main damping mechanism. In both cases, the 1/r law of pressure attenuation through the liquid was not affected by the viscoelastic properties of the liquid.

Brujan [30] noted that in order to gain a full understanding of the behaviour of cavitation bubbles in non-Newtonian liquids, it is necessary to extend theoretical studies to the case of asymmetric collapse of bubbles since some experiments have indicated that the effect of fluid viscoelasticity is more evident in bubbles collapsing in the neighbourhood of a solid boundary, altering the intensity of the liquid jet directed toward to boundary.

The present study follows a similar approach to the one employed by Wang et al. [16] and seeks to extend previous studies on modelling EMBs forced by ultrasound by determining the effects of viscoelasticity and shell properties on (potentially non-spherical) bubble dynamics. In a recent study, Wu et al. [31] also consider bubble shell properties but modelled through a finite element method coupled with a boundary element method at the

bubble-shell interface. Non-spherical bubble interaction with a solid boundary is considered but the ambient flow remains invisicid (and irrotational). Similarly, Heidary et al. [32] consider EMB dynamics adjacent to deformable (blood vessel) walls including the effects of ultrasound, but, again, the ambient fluid is considered Newtonian. The present study is therefore distinct by modelling the viscoelastic rheology of the ambient fluid in combination with a shell model and acoustic forcing.

Viscoelasticity is modelled using the Oldroyd B model which is able to account for both solvent and polymeric behaviour. This model is able to describe a range of viscoelastic behaviour and can be implemented within the boundary element methodology, noting certain approximations (discussed in Section 2 below). The numerical approach is used to predict the dynamics of an EMB located near a rigid wall following its excitation by an ultrasound field. The mathematical models for spherical EMBs, based on a modified Rayleigh-Plesset equation, and non-spherical EMBs, using a modified Bernouilli equation, are described in Section 2. This is followed in Section 3 by a description of a non-singular boundary element method that removes the singularity in the kernel. Numerical results are presented in Section 4 in which the effects of shell width, viscoelasticity and ultrasound properties on bubble dynamics are described. Finally, some concluding remarks are made in Section 5.

2. Mathematical Model

The aim of the present study is to understand how viscoelasticity of the fluid and the shell affects the non-spherical dynamics of encapsulated microbubbles in a viscoelastic fluid forced by ultrasound. Heat and mass transfer are not modelled explicitly in this paper; conditions are assumed adiabatic and hence the polytropic law is used to model the gas in the bubble. Szeri et al. [33] investigated the effects of heat and mass transfer on bubble dynamics during the violent collapse of non-spherical bubbles and compared them with the predictions of a simplified model which excluded these effects. They found that although the qualitative evolution of the bubble was similar in both cases, it grows larger and collapses later for the model which includes the heat and mass transfer.

2.1. Bubble Dynamics for Spherical EMBs

It is well known that the oscillations of a clean/shell-free, spherical bubble in an infinite expanse of incompressible fluid can be described by the Rayleigh-Plesset equation. The Rayleigh-Plesset equation originates from the work of Rayleigh [34] on the (inviscid) collapse of an empty cavity or void. Several extensions to the Rayleigh-Plesset equation have been proposed to describe spherical encapsulated bubbles. Although the focus of the present paper is on the numerical prediction of nonspherical bubble dynamics, a model for spherical dynamics is considered solely for validation purposes.

We assume that the shell is a linear, incompressible viscoelastic solid of thickness ϵ . Let R(t) denote the outer radius of the shell at time t. We assume $\epsilon \ll R$ [35]. A Rayleigh-Plesset equation can be derived by integrating the radial component of the momentum equation

$$\rho \left(\frac{\partial u}{\partial t} + u \frac{\partial u}{\partial r} \right) = -\frac{\partial p}{\partial r} + \frac{\partial T_{rr}}{\partial r} + 3 \frac{T_{rr}}{r}, \tag{1}$$

over $[R-\epsilon,\infty)$ where the radial velocity component is given by

$$u = \frac{R^2 \dot{R}}{r^2}. (2)$$

In Eq. (1), p is pressure, ρ is density and T_{rr} is the radial stress component. We generalize the contributions of Church [8] and Hoff [9], for example, to model a bubble in an infinite expanse of viscoelastic fluid. The radial stress component in the shell $(R - \epsilon \leq r \leq R)$ and fluid $(R \leq r)$ is modelled as follows (see Allen and Roy [25, 26] and Church [8]).

$$T_{rr} = \begin{cases} (\lambda_s + 2\chi_{sh}) \frac{\partial \epsilon_{rr}}{\partial r} + 2\lambda_s \frac{\epsilon_{rr}}{r} + 2\mu_{sh} \frac{\partial u}{\partial r} & R - \epsilon \le r \le R, \\ 2\mu \frac{\partial u}{\partial r} + \tau_{rr} & R \le r, \end{cases}$$
(3)

where λ_s and χ_{sh} are the Lamé constants, μ_{sh} is the viscosity of the shell, μ is the dynamic viscosity of the fluid, ϵ_{rr} is the radial component of the strain tensor and τ_{rr} is the radial component of the polymeric contribution to the stress tensor in the fluid. The second Lamé constant is also known as the modulus of rigidity.

The model assumes that the shell thickness remains constant in time [36] and does not change with variations in volume. Wang et al. [16] argued that the simplified model can be used to approximate the essential effects of the coating since the EMB is usually approximately spherical during most of its lifetime except for a short period during the end of collapse. Thus the model is able to provide a good estimate of the influence of the shell on the bubble, the asymmetric flow and pressure fields prior to jet development. When liquid jetting starts, the large asymmetric momentum of the liquid flow and high pressure of the bubble gas are the dominant effects; the elastic and viscous effects of the thin coating should be secondary effects.

Church [8] provides an expression for ϵ_{rr} in the limit of small displacements from which the pressure difference, ΔP , across the shell, which is the contribution of the integral of the last term in Eq. (1) over the shell, can be determined

$$\Delta P = -\frac{12\epsilon}{R_0^2} \left(\frac{R_0}{R}\right)^2 \left[\chi_{sh}(R - R_0) + \mu_{sh}\dot{R}\right].$$

The force balance at the gas/shell interface gives

$$p_s|_{R-\epsilon} = p_q + T_{s,rr}|_{R-\epsilon} - \sigma_q C_{R-\epsilon},\tag{4}$$

while the corresponding force balance at the shell/liquid interface yields

$$p_b = p_s|_R - T_{s,rr}|_R - \sigma_s C_R + T_{l,rr}|_R.$$
 (5)

where p_b is the pressure on the liquid side of the interface, p_s is the pressure within the shell, p_g is the internal gas pressure, σ_g and σ_s are the surface tension coefficients at the two interfaces, and C denotes curvature. Note that the expression for capillary pressure derived in the paper of Glazman [37] and implemented in subsequent studies, e.g. Morgan et al. [35], contained an error which was reported by Marmottant et al. [10]. The correct expression is employed here.

Using the polytropic law

$$p_g \left(\frac{4}{3}\pi R^3\right)^{\kappa} = \text{constant},\tag{6}$$

where κ is the ratio of specific heats for the gas in association with Eq. (4) with initial conditions $R = R_0$, $\dot{R} = 0$ and $T_{rr} = 0$ at t = 0 we can derive the following expression for the internal gas pressure

$$p_g = \left(p_0 + \frac{2\sigma}{R_0}\right) \left(\frac{R_0}{R}\right)^{3\kappa},\tag{7}$$

where p_0 is hydrostatic pressure. Finally, integrating Eq. (1) over $[R - \epsilon, \infty)$ and using the above results we arrive at the modified Rayleigh-Plesset equation

$$R\ddot{R} + \frac{3}{2}\dot{R}^{2} = \frac{1}{\rho} \left[\left(p_{0} + \frac{2\sigma}{R_{0}} \right) \left(\frac{R_{0}}{R} \right)^{3\kappa} - \frac{4\mu\dot{R}}{R} - \frac{2\sigma}{R} - \frac{12\epsilon}{R_{0}^{2}} \left(\frac{R_{0}}{R} \right)^{2} \left[\chi_{sh}(R - R_{0}) + \mu_{sh}\dot{R} \right] + 3\int_{R}^{\infty} \left(\frac{\tau_{rr}}{r} \right) - p_{\infty}(t) \right].$$
(8)

where $\sigma = \sigma_g + \sigma_s$ since $C|_{R-\epsilon} = C|_R$ for a spherical EMB.

2.2. Bubble Dynamics for Nonspherical EMBs

2.2.1. Assumptions and Justifications

Consider an initially spherical bubble whose centroid is a distance h from a horizontal rigid boundary of infinite extent. The bubble is assumed to remain axisymmetric in time since this is generally found to be the case for small cavitation bubbles [38]. Additionally, it is the axisymmetric configuration that generates maximum jet speeds and pressures and thus provides an indication of the maximum potential damage to nearby surfaces.

The fluid flow is assumed to be irrotational. In order to formulate a velocity potential, ϕ , which satisfies Laplace's equation, it is necessary to assume incompressibility. The primary condition needed for this approximation to be valid is

$$M^2 \ll 1, \tag{9}$$

where M = U/c is the Mach number, c is the speed of sound in the liquid and U is the magnitude of variations of the fluid velocity with respect to both position and time [39]. Note that in the late stages of collapse when a jet forms the bubble wall velocities can approach the speed of sound which means that condition (9) is violated and liquid compressibility can no longer be ignored. These high velocities also give rise to very large pressures in the fluid. Theoretical studies by [40] confirmed that the effects of compressibility can be important, particularly in the late stages of collapse. However, in order to gain some appreciation of the bubble motion we follow the majority of other works in the literature (see Pearson et al. [41], for example), and assume only a small fraction of bubble kinetic energy is radiated away as sound, and so impose incompressibility.

Regarding the irrotational assumption, there is a long-held and widespread misconception that irrotational motion implies inviscid flow. In a comprehensive series of works, Joseph and co-workers (see for example, Joseph [42]) have campaigned and repeatedly demonstrated the utility of both viscous and viscoelastic irrotational flows. While internal viscous effects may vanish, viscosity and viscoelasticity are inherent fluid properties and reappear in the governing equations when applying stress boundary conditions. Such boundary conditions are typically applied at free-surfaces, where vorticity generation is weaker relative to no-slip conditions, and hence for free-surface flows (even with viscous/viscoelastic effects) irrotational flows can provide good approximations to full Navier-Stokes solutions. Indeed, Batchelor [39] (Chap. 5, p. 366) notes that at free-surfaces the variation in velocity from irrotational across the boundary layer can be relatively small. It has further been shown, depending on the test case, that the irrotational approximation can hold for surprisingly viscous flows with good agreement to experiment even for Reynolds number Re = 0.1 [43]. Clearly, retaining viscous and/or viscoelastic effects in irrotational flows can provide useful quantitative insight, and is a modelling approach that has been adopted previously for a range of bubble/drop problems. For example, Georgescu et al. [44] model a bursting bubble assuming irrotationality and including viscous effects, noting the reduction in jet speed and height with increasing viscosity. Related irrotational flow studies that consider the effect of viscosity include studies on drop oscillation [45], spherical cap bubbles [43], the viscous Kelvin-Helmholtz instability [46], and buoyant bubbles near walls [47]. Rayleigh-Taylor instabilities in viscoelastic (Oldroyd B) drops have also been studied using viscoelastic potential flow [48] with good agreement obtained with complete/rotational theoretical flow analysis. The above works are in addition to the seminal papers of Blake and co-workers [49, 50, 51, 52, 53, 54], amongst others, which, although setting a zero viscosity, provide additional examples of the capabilities of the irrotational approximation in modelling real flows.

Following the above justification, we assume that viscous/viscoelastic effects in the fluid bulk are negligible and that the effects of fluid rheology appear only at the bubble surface, and thus can be modelled approximately through the bubble interface boundary condition [39]. We reiterate that this approximation has been used to good effect in studies mentioned above and previously in Lind and Phillips [20, 55, 56, 57] and Walters [58].

2.2.2. The Mathematical Model

Let us state mathematically the key assumptions of incompressibility ($\nabla \cdot \mathbf{u} = 0$) and irrotationality ($\nabla \times \mathbf{u} = 0$), for a fluid velocity \mathbf{u} . By standard theorems in vector calculus there then exists a velocity potential, ϕ , that satisfies Laplace's equation:

$$\nabla^2 \phi = 0. \tag{10}$$

We assume the fluid is at rest far from the bubble and hence require $\phi \to 0$ (and subsequently $\mathbf{u} \to 0$) as $r \to \infty$. Well-known general solutions exist for ϕ , and in the axisymmetric configuration considered here, the potential then has the form $\phi \sim 1/r$ to leading order, for some radial distance r from the bubble. Note, the potential, velocity, and stresses decay with distance from the bubble with increasing rapidity, respectively (due to increasing powers of 1/r). Consider the general equation of motion,

$$\rho \frac{D\mathbf{u}}{Dt} = -\nabla p + \nabla \cdot \boldsymbol{\tau},\tag{11}$$

where $\boldsymbol{\tau}$ is the extra stress. This equation may admit a fully irrotational counterpart if the divergence of the extra stress can be expressed as the gradient of a scalar, i.e. if $\nabla \cdot \boldsymbol{\tau} = \nabla \psi$, for some scalar ψ [59]. This is trivially the case if $\nabla \cdot \boldsymbol{\tau} = 0$ and this occurs exactly for a viscous fluid and a linear viscoelastic fluid for a general potential. We persist with this assumption here and set $\nabla \cdot \boldsymbol{\tau} = 0$ (i.e. viscous/rheological contributions in the fluid bulk are negligible, as previously argued in Section 2.2.1). Whilst exactly zero for linear viscoelastic models, in Section 2.2.3 we make the case for the approximate use of setting $\nabla \cdot \boldsymbol{\tau} = 0$ for nonlinear models, given the necessarily rapid decay in nonlinear terms in the stress with distance from the bubble. Using $\nabla \phi = \mathbf{u}$ with (11), applying 'at rest' conditions in the far-field (where pressure is p_{∞}), for a cavitation bubble with a 'clean' (shell-free) surface, the pressure on the fluid side of the bubble interface, p_b is then given by

$$p_b = -\rho \frac{\mathrm{D}\phi}{\mathrm{D}t} + \frac{\rho}{2} |\nabla \phi|^2 + p_{\infty}, \tag{12}$$

where $\mathrm{D}/\mathrm{D}t$ is the material derivative. If we assume there is no mass transfer through the bubble wall then balancing normal forces across the surface results in

$$p_b = p_g + \tau_{nn} - \sigma C, \tag{13}$$

where C is the local curvature of the bubble surface, σ is the surface tension coefficient, and p_g is the internal pressure of the bubble, given by

$$p_g(t) = p_0 \left(\frac{R_0}{R}\right)^{3\kappa},\tag{14}$$

where p_0 is the (initial) internal gas pressure. Note it is through (13) that any fluid viscoelastic effects influence the bubble by means of the normal stress component, τ_{nn} . To account for the shell, Eq. (13) is modified in the following way

$$p_b = p_q + \tau_{nn} - \sigma C + \Delta P. \tag{15}$$

Combining (12) and (15) to eliminate p_b gives the Bernoulli equation, which is used to update ϕ on the bubble surface

$$\rho \frac{\mathrm{D}\phi}{\mathrm{D}t} = \frac{\rho}{2} |\nabla \phi|^2 - \tau_{nn} + \sigma C - \Delta P + p_{\infty} - p_g, \tag{16}$$

where t is time. To model an EMB using the boundary element method, a generalisation of the spherical model described in the previous section is developed. In the case of a spherical bubble, the pressure over the bubble surface is spatially constant at each instant in time whereas for a non-spherical bubble the pressure varies locally over the bubble surface. In the boundary element method, the bubble surface is decomposed into a number (N) of segments separated by N+1 nodes. To modify the equations for a non-spherical bubble the radius R is replaced by the local radius $R_c(s)$ at each node where s denotes arclength. This can be calculated using $R_c(s) = 1/C(s)$ where C(s) is the local radius of curvature defined by

$$C(s) = -\frac{(r'(s)z''(s) - z'(s)r''(s))}{(r'(s)^2 + z'(s)^2)^{3/2}},$$
(17)

where r(s) and z(s) are the coordinates of nodes on the bubble surface. The derivatives in Eqn. (17) can be determined by constructing quintic spline representations for r(s) and z(s). The pressure at each node is then calculated using

$$p_{b} = \left(p_{0} + \frac{2\sigma}{R_{0}}\right) \left(\frac{R_{0}}{R_{c}}\right)^{3\kappa} - \frac{2\sigma}{R_{c}} + \tau_{nn}$$
$$-\frac{12\epsilon}{R_{0}^{2}} \left(\frac{R_{0}}{R_{c}}\right)^{2} \left[\chi_{sh}(R_{c} - R_{0}) + \mu_{sh}\dot{R}_{c}\right]. \tag{18}$$

R with the local quantity $R_c(s)$ at each node. In the same manner as the interfacial term, the radius R is replaced by $R_c(s)$ and the velocity, \dot{R} , becomes $\partial \phi / \partial n$ in the viscous shell damping term. Accordingly, the Bernoulli equation used to update ϕ for a non-spherical EMB is

$$\rho \frac{\mathrm{D}\phi}{\mathrm{D}t} = p_{\infty} - \left(p_0 + \frac{2\sigma}{R_0}\right) \left(\frac{R_0}{R}\right)^{3\kappa} + \frac{\rho}{2} |\nabla\phi|^2$$

$$- 2\eta_s \frac{\partial^2\phi}{\partial n^2} - \tau_{nn} + \frac{2\sigma}{R_c}$$

$$+ \frac{12\epsilon}{R_0^2} \left(\frac{R_0}{R_c}\right)^2 \left[\chi_{sh}(R_c - R_0) + \mu_{sh} \frac{\partial\phi}{\partial n}\right], \tag{19}$$

where V_0 is the initial bubble volume, V is the bubble volume and η_s is the solvent viscosity. The bubble surface must also be updated in time. Since the bubble surface is a material surface, fluid particles which begin on the surface will remain there and thus the surface can be updated in a Lagrangian manner using

$$\frac{\mathbf{D}\mathbf{x}}{\mathbf{D}t} = \nabla\phi,\tag{20}$$

where \mathbf{x} is a point on the bubble surface. To integrate Eqns. (19) and (20) in time, a constitutive equation must be chosen for the stress while the normal velocities $\partial \phi / \partial n$ are determined by solving a boundary integral equation.

2.2.3. Modelling Viscoelasticity

Finally, a constitutive equation is required to provide a relationship between stress and strain. One of the aims of this paper is to understand the effects of viscoelasticity on bubble dynamics. Therefore, fluid rheology is modelled using the Oldroyd-B model, which is chosen because it is sophisticated enough to model a range of rheological behaviour. The model predicts stress relaxation, constant shear viscosity and quadratic first normal stress difference. Brujan et al. [60] have shown that shear-thinning is not important when studying bubble dynamics and collapse. In experiments investigating the bubble dynamics of shear-thinning polymeric solutions, they showed that dynamics can be described by simply taking the infinity-shear viscosity as the viscosity of the polymer solution.

For the Oldroyd-B model the extra stress au can be decomposed in terms of its solvent and polymeric contributions

$$\boldsymbol{\tau} = \boldsymbol{\tau}^s + \boldsymbol{\tau}^p,\tag{21}$$

where

$$\boldsymbol{\tau}^s = 2\eta_s \nabla \mathbf{u}, \quad \boldsymbol{\tau}^p + \lambda \boldsymbol{\tau}^p = 2\eta_p \nabla \mathbf{u}.$$
 (22)

In these equations η_s , η_p and λ are the solvent viscosity, polymeric viscosity and relaxation time of the fluid, respectively. The superscripts s and p denote solvent quantities and polymer quantities. In terms of the normal stress component τ_{nn} the relevant equations for the solvent and polymeric contributions to the stress become

$$\tau_{nn}^s = 2\eta_s \frac{\partial^2 \phi}{\partial n^2},\tag{23}$$

$$\lambda \frac{D\tau_{nn}^p}{Dt} = -\tau_{nn}^p - 2\lambda \tau_{nn}^p \frac{\partial^2 \phi}{\partial n^2} - 2\eta_p \frac{\partial^2 \phi}{\partial n^2}.$$
 (24)

As mentioned in Section 2.2.2, there are compatibility requirements for viscoelastic models to support a general irrotational flow [59] - namely $\nabla \cdot \boldsymbol{\tau}$ $\nabla \psi$, for some scalar ψ . Linear viscoelastic models are always compatible with any irrotational flow (as $\nabla \cdot \boldsymbol{\tau} = 0$), but the more popular and widespread non-linear models (such as Oldroyd B where non-linearity appears in the upper-convected derivative) do not support all potential flows exactly (the radially symmetric Rayleigh-Plesset flow, however, is a potential flow compatible with any viscoelastic model). Nevertheless, the importance / prevalence of the non-linear Oldroyd B model is such that it may be applied here in an approximate sense noting that the non-linear terms tend to zero extremely quickly with increasing distance from the bubble surface. For example, since it is required that $\phi \to 0$ with increasing radial distance from the bubble (i.e. as $r \to \infty$), via the analytical general solution for Laplace's equation under axisymmetry, velocity gradient and stress terms must decrease like $1/r^3$ to leading order. The non-linear terms in the Oldroyd B model must then decrease at least as fast as $1/r^6$. The model, therefore, tends to exact compatibility with a general irrotational flow extremely quickly. This supports the modelling approximation used here that viscoelastic effects are most significant at bubble surface and negligible in the fluid bulk.

2.2.4. Summary of Modelling Assumptions

For clarity, we summarise the modelling assumptions used to describe non-spherical bubble dynamics in this work, following the detailed discussion and justification above. In particular:

• The flow domain is assumed to be axisymmetric.

- The flow is assumed to be irrotational, incompressible and isothermal.
- Viscoelastic effects in the fluid bulk are neglected ($\nabla \cdot \boldsymbol{\tau} = 0$, everywhere), as this term tends to zero extremely quickly due to rapid decay in the potential. It is also exactly zero for linear viscoelastic models in any irrotational case.
- Remaining viscoelastic effects appear directly in the stress balance at the bubble surface, as in viscous irrotational models.
- The viscoelastic extra stress is governed by the Oldroyd B model.

3. Non-Singular BEM Formulation

In the standard BEM formulation, the potential satisfies the boundary integral equation (see, for example, Taib [61])

$$c(\mathbf{p})\phi(\mathbf{p}) = \int_{\partial\Omega} \left(\frac{\partial\phi}{\partial n}(\mathbf{q})G(\mathbf{p}, \mathbf{q}) - \phi(\mathbf{q}) \frac{\partial G}{\partial n}(\mathbf{p}, \mathbf{q}) \right) dS, \tag{25}$$

where $c(\mathbf{p})$ is a piecewise constant, Ω and $\partial\Omega$ are the fluid domain and its boundary, respectively, and \mathbf{p} , \mathbf{q} are points in the fluid and on the boundary, respectively. To solve (25) numerically, the bubble surface is discretised into N segments and (25) is collocated at points $\mathbf{p} = \mathbf{p}_i$, $i = 1, \ldots, N+1$,

$$c(\mathbf{p}_{i})\phi(\mathbf{p}_{i}) + \sum_{j=1}^{N} \int_{s_{j}}^{s_{j+1}} \phi(\mathbf{q}) \frac{\partial G}{\partial n}(\mathbf{p}_{i}, \mathbf{q}) dS$$

$$= \sum_{j=1}^{N} \int_{s_{j}}^{s_{j+1}} \frac{\partial \phi}{\partial n}(\mathbf{q}) G(\mathbf{p}_{i}, \mathbf{q}) dS, \qquad (26)$$

where s_j is the arclength of the bubble surface at node j and the known quantities are on the left-hand side. Given the potential ϕ at each node, Eqn. (26) can be used to solve for the normal velocities $\partial \phi(\mathbf{p}_i)/\partial n$. However, when an integral over a segment in (26) contains the collocation point \mathbf{p}_i , both G and $\partial G/\partial n$ will possess a singularity. Following Sun et al. [62], singularities are removed from the boundary integral equation by defining new variables

$$\psi_i(\mathbf{p}) = \phi(\mathbf{p}_i) + \left(\frac{\partial \phi}{\partial n}\right)_i f_i(\mathbf{p}),$$
 (27)

for i = 1, ..., N + 1, where the functions f_i are constructed to satisfy

$$\nabla^2 f_i(\mathbf{p}) = 0, \quad f_i(\mathbf{p}_i) = 0, \quad \frac{\partial f_i}{\partial n}(\mathbf{p}_i) = 1.$$
 (28)

Writing an integral equation for the new variables and subtracting it from (25) a non-singular formulation of the integral equation can be derived (see [63])

$$\int_{S} \left[\phi(\mathbf{q}) - \phi(\mathbf{p}_{i}) \right] \frac{\partial G}{\partial n}(\mathbf{p}_{i}, \mathbf{q}) dS = \int_{S} \frac{\partial \phi}{\partial n} G(\mathbf{p}_{i}, \mathbf{q})
+ \left(\frac{\partial \phi}{\partial n} \right)_{i} \int_{S} \left(f_{i}(\mathbf{q}) \frac{\partial G}{\partial n}(\mathbf{p}_{i}, \mathbf{q}) - \frac{\partial f_{i}}{\partial n}(\mathbf{q}) G(\mathbf{p}_{i}, \mathbf{q}) \right) dS.$$
(29)

The careful construction of the functions f_i , satisfying the properties described by (28) ensures that singularities present in G and $\partial G/\partial n$ are removed.

For a bubble near a rigid wall, the no-penetration condition at the wall results in the following form for the functions f_i , given by

$$f_i(\mathbf{p}) = -\frac{\rho_i^3 \bar{\rho}_i^3}{\bar{\rho}_i^3 \beta_i + \rho_i^3 \bar{\beta}_i} \left[\left(\frac{1}{\rho} - \frac{1}{\rho_i} \right) + \left(\frac{1}{\bar{\rho}} - \frac{1}{\bar{\rho}} \right) \right], \tag{30}$$

where

$$\rho = \sqrt{r^2 + (z - z_D)^2}, \quad \bar{\rho} = \sqrt{r^2 + (z + z_D)^2},
\beta = rn_r + (z - z_D)n_z, \quad \bar{\beta} = rn_r + (z + z_D)n_z,$$
(31)

and the suffix i indicates evaluation at the point $(r_i, 0, z_i)$. In this representation $\mathbf{p}_D = (0, 0, z_D)$ is chosen to be any point located outside the domain, provided that $\mathbf{n}_i \cdot (\mathbf{p}_i - \mathbf{p}_D) \neq 0$. The point \mathbf{p}_D is chosen to be located on the z-axis to ensure that ψ_i defined by (27) are axisymmetric functions. This ensures that the functions f_i are constant in θ and therefore do not appear in the azimuthal integrals contained in (29). Full details of this derivation can be found in Walters [63] where the effects of viscoelasticity on a clean, unforced cavitation bubble are studied using this approach.

To discretise the bubble surface, quintic splines are chosen. The surface variables, potential and extra stress are represented in each segment (s_i, s_{i+1}) by a fifth-order polynomial. Quintic splines have been shown to be more accurate and stable than cubic splines [63]. To attain a prescribed level of

accuracy far fewer nodes are required when quintic splines are used. The BEM formulation above has also been extended to accommodate changes in bubble topology (i.e. the creation of toroidal bubbles). In the present study no toroidal bubbles are formed over the parameter ranges considered, but further information on the procedure used to model toroidal bubbles (using the vortex ring method) can be found in Walters [58] and Wang et al. [64].

3.1. Modelling the Ultrasound Pressure Field

To simulate the interaction between ultrasound and an encapsulated bubble, a Gaussian acoustic pulse is used. The pulse is assumed to be much larger than the bubble and is thus approximated as being infinitely large in the direction perpendicular to the wave propagation. This pulse is incorporated into the model by modifying the pressure term $p_{\infty}(\mathbf{x},t)$. The explicit form for the static Gaussian pulse acting uniformly in space is

$$p_{\infty}(t) = p_0 + p_A \sin[2\pi f(t - t_p)] \exp[-\pi^2 l^2 f^2 (t - t_p)^2], \tag{32}$$

where p_A is the maximum amplitude of the pulse, f is the frequency, t_p is the centre of the pulse and l is the width of the pulse. Fig. 1 shows the pressure pulse as a function of time at a fixed point in space for f=2 MHz and $p_A=200$ kPa.

The above static pulse is used for the validation cases in Sec. 4. For the main results in Sec. 5 the case of a dynamic (travelling) pulse is considered, where it is assumed that the centre of the pulse, $z_m(t)$, moves downwards with a constant speed $\dot{z}_m(t) = f\lambda_p$. The pulse wavelength, λ_p , is selected to be larger but within an order of magnitude of R_0 so that bubble and pulse interact on similar spatial scales, eliciting a highly dynamic bubble response. The pressure due to the pulse at a node $\mathbf{x}_i = (r_i, z_i)$ on the bubble surface at time t is given by

$$p_{\infty}(\mathbf{x}_i, t) = p_0 + p_A \sin[z_i - z_m(t)] \exp\left[-\frac{l^2}{4}(z_i - z_m(t))^2\right].$$
 (33)

The initial position of the centre of the pulse is chosen to be far from the bubble and is given by $z_m(0) = 27R_0$. The low pressure component of the pulse interacts with the bubble initially causing the bubble to expand and rise. Subsequently, the bubble moves towards the rigid wall in response to the high pressure component of the pulse. It is assumed that the pulse is reflected entirely from the wall (z = 0) and subsequently interacts with the bubble a second time. The bubble is therefore affected by the superposition of both incident and reflected pulses.

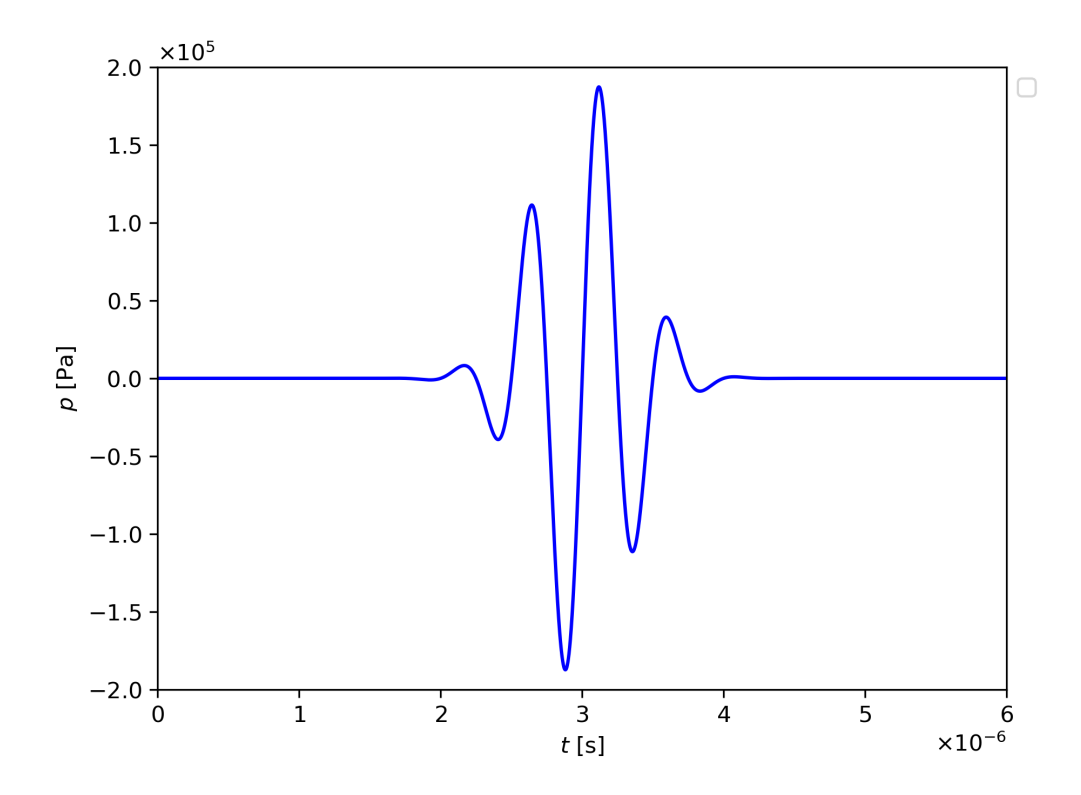


Figure 1: Evolution of a typical Gaussian pressure pulse at a fixed point in space with $p_0=0$ kPa, $p_A=200$ kPa, f=2 MHz, $t_p=3.0$ μs and l=1/3

3.2. Reynolds and Deborah numbers

Although the governing equations and solutions are presented in dimensional form, a Reynolds and Deborah number can be defined to aid interpretation of the results. The pulse frequency can be used to provide a pertinent characteristic time scale and the initial bubble radius provides the characteristic length. Accordingly, the Reynolds (Re) and Deborah (De) numbers can be defined, respectively, by

$$Re = \frac{\rho \omega_{\text{ref}} R_0^2}{(\eta_{\text{s}} + \eta_{\text{p}})}, \quad De = \lambda \omega_{\text{ref}},$$
 (34)

where ω_{ref} is a characteristic frequency and R_0 is the initial bubble radius. Here we choose $\omega_{\text{ref}} = 2$ MHz and $R_0 = 1$ μ m (typical real-life ultrasound frequency and microbubble radius values, respectively [1, 2]). Considering blood plasma as the ambient fluid in a practical biomedical context, measurements of viscosity and (maximum) relaxation time typically yield values of O(1 mPas) and $O(10^{-4} \text{ s})$, respectively [65]. Accordingly, this paper explores Reynolds numbers around O(1) and Deborah numbers up to De = 10 (but below the experimental maximum) to be representative of the physical problem. The viscosity ratio is defined to be

$$\beta = \frac{\eta_{\rm s}}{\eta_{\rm s} + \eta_{\rm p}}.$$

All simulations in this paper were performed with $\beta = 0.8$.

4. Comparison of BEM with the Spherical Model

The numerical results presented in this section use the following values for the initial internal gas pressure, the ratio of specific heats for the gas, shell thickness, surface tension, shell viscosity and elasticity modulus of shell, respectively, for the encapsulated microbubble, unless otherwise stated,

$$p_0 = 101 \text{ kPa}, \ \kappa = 1.07, \ \varepsilon = 1 \text{ nm},$$

 $\sigma = 0.051 \text{ N/m}, \ \mu_{sh} = 1 \text{ Pas}, \ \chi_{sh} = 0.5 \text{ Pa}.$ (35)

These values are taken from Wu et al. [66] and were obtained using a mean square errors best fit for experimentally obtained values for the phospholipid contrast agent MP1950 filled with a decafluorobutane gas. This is a thin lipid-shelled contrast agent that prevents the gas from leaking out of the bubbles. It also introduces an additional elasticity for the bubbles' radial oscillations. The shell has a thickness of the order of a few nanometres.

The system of equations is integrated using a fourth-order Runge-Kutta time stepping scheme. The time step is chosen to be

$$\Delta t = \frac{\Delta t_{\text{max}}}{\max(\mathrm{D}\phi/\mathrm{D}t)},\tag{36}$$

where $\triangle t_{\rm max}$ is the maximum time step. The time step has been chosen to deal with the rapidly changing velocity that can occur during bubble collapse; for large velocities the time step is reduced in order to capture the high speed dynamics of the bubble. All calculations reported in this paper were conducted on a desktop computer with a Core i7-10700 CPU and 32GB RAM.

The predictions of the BEM model are compared with the solution of the spherical model (8) for an encapsulated microbubble forced by a Gaussian pulse with parameters: $p_A = 200$ kPa, f = 1 MHz, Re = 6.3, De = 0 and $R_0 = 1$ μ m in the absence of a rigid wall. Figs. 2 and 3 provide comparisons of the pressure and the equivalent bubble radius, respectively. The pressure of the pulse for the BEM code is measured at the north pole of the bubble (the axial node at r = 0 with the maximal z position value at t = 0) and the 'equivalent bubble radius' is defined by

$$R_{eq} = \left(\frac{3V(t)}{4\pi}\right)^{1/3} \tag{37}$$

where V(t) is the volume of the bubble at time t. Convergence of the approximation generated using the BEM model with respect to the number of nodes on the bubble surface, n_p , and $\Delta t_{\rm max}$, is also demonstrated in these figures.

There is excellent agreement between the predictions obtained using the spherical model and the implementation of BEM with the pressure pulse acting on the bubble surface simultaneously. For the combination of discretization parameters $(n_p, \Delta t_{\text{max}}) = (40, 1.59 \times 10^{-4})$, $(80, 1.59 \times 10^{-5})$, $(40, 1.59 \times 10^{-6})$, the equivalent bubble radius is only slightly different from the spherical model shown in Fig. 3. The pressure and the equivalent bubble radius for the other combinations of n_p and Δt_{max} are in complete agreement with the spherical model. Therefore, for the remainder of the paper we have chosen to use $n_p = 40$ and $\Delta t_{\text{max}} = 1.59 \times 10^{-5} \mu \text{s}$ as a good compromise between computational expense in terms of CPU time shown in Table 1 and accuracy of the numerical approximation as evidenced by the data shown in Figs. 2 and 3.

Next we consider the situation in which the bubble is allowed to translate dynamically in response to the imparted energy from the pressure pulse and make comparisons with the static situation in which the pressure pulse acts on all points on the bubble surface simultaneously. The comparisons for the pressure at the north pole of the bubble, p, and equivalent bubble radius, R_{eq} , are shown in Figs. 4 and 5, respectively. Similar responses are predicted initially. Subsequently, after around $t = 1 \mu$ s there is a significant difference in behaviour, with the dynamic case eventually displaying sustained higher frequency oscillations in both pressure and equivalent bubble radius. As the bubble moves downwards in response to the pressure pulse it eventually

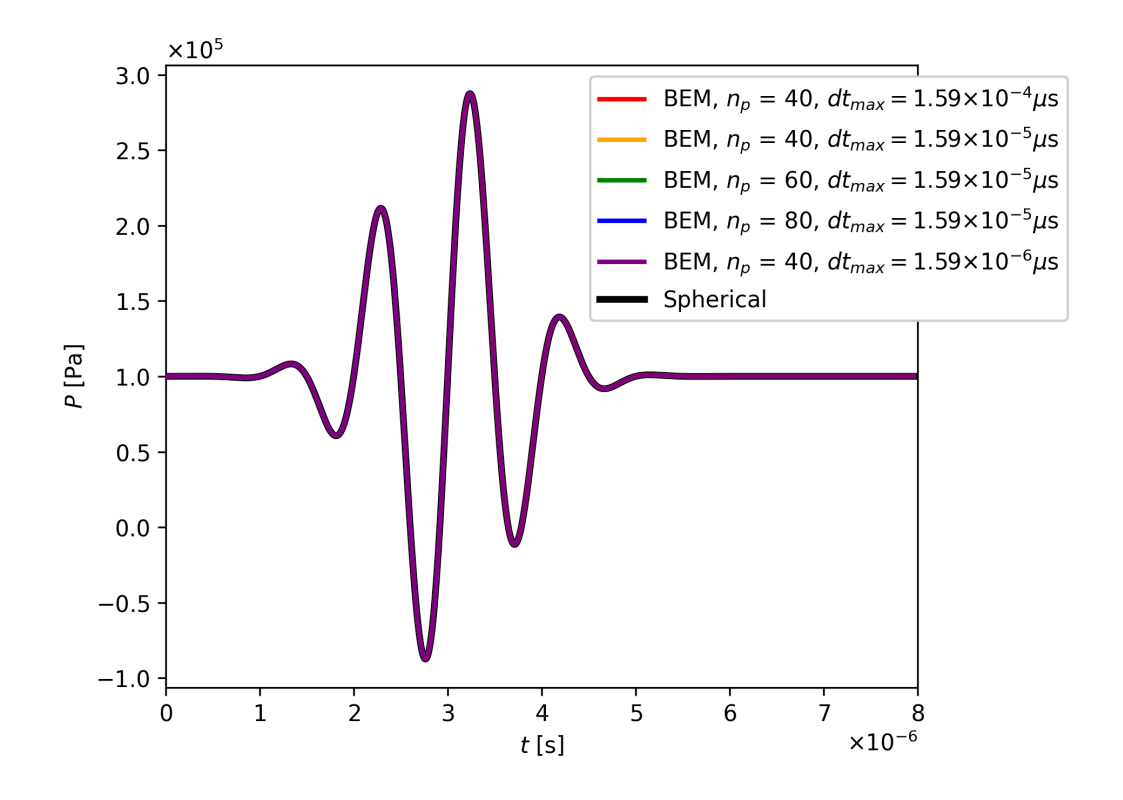


Figure 2: Comparison of BEM with spherical model with respect to the pressure at the north pole for an EMB forced by a Gaussian pressure pulse with Re=6.3, De=0, $R_0=1$ μm , $\varepsilon=1$ nm, $\sigma=0.051$ N/m, h=0 μm , $p_A=200$ kPa and f=1 MHz.

expands and oscillates about a steady state equivalent bubble radius almost 50% larger than its initial value (Fig. 5). This can be seen in the snapshots of the bubble profiles in Fig. 6 where it can also be seen that the bubble retains an almost spherical shape throughout the duration of the simulation.

In the next set of results the maximum amplitude of the pressure pulse is decreased and the frequency is increased. Figs. 7 and 8 show the evolution of the equivalent bubble radius, R_{eq} , and centroid, z_c , respectively, for $p_A = 100$ kPa, f = 2 MHz, Re = 6.3 and $R_0 = 1$ μ m. The BEM prediction with the pressure pulse acting at all points on the bubble surface simultaneously is in excellent agreement with the spherical model which is to be expected. This further validates the BEM model. In the more realistic case in which the pressure pulse translates, differences in the predictions emerge. There is now a delay in the peak amplitude of the bubble response. The maximum equiv-

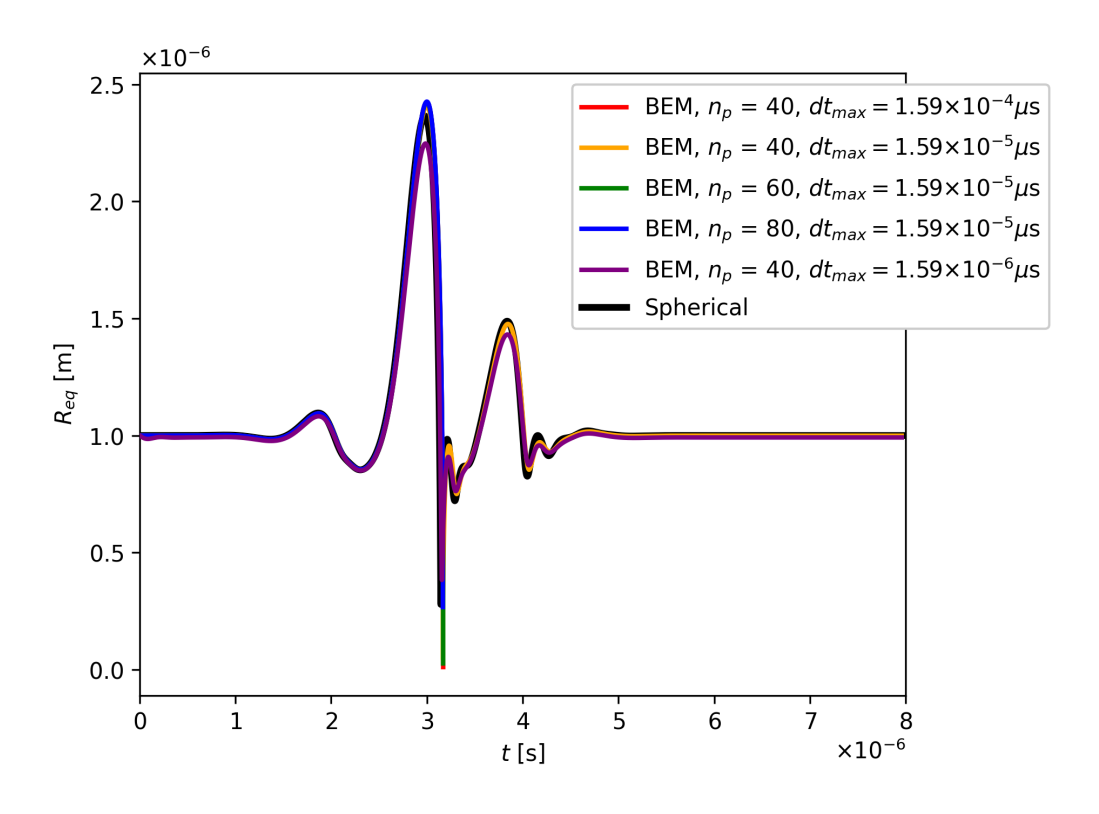


Figure 3: Comparison of BEM with spherical model with respect to the equivalent bubble radius for an EMB forced by a Gaussian pulse with $Re=6.3,\,De=0,\,R_0=1$ µm, $\varepsilon=1$ nm, $\sigma=0.051$ N/m, h=0 µm, $p_A=200$ kPa and f=1 MHz.

Table 1: Dependence of the CPU time on spatial and temporal discretization parameters for the evaluation of EMB dynamics forced by a Gaussian pulse with $p_A=200 \mathrm{kPa},\,f=1$ MHz, Re=6.3 and $R_0=1~\mu\mathrm{m}$.

Method	$n_{\rm p}$	$\Delta t_{\rm max}(\mu { m s})$	CPU time (min)
BEM	40	1.59×10^{-4}	15
BEM	40	1.59×10^{-5}	134
BEM	60	1.59×10^{-5}	298
BEM	80	1.59×10^{-5}	528
BEM	40	1.59×10^{-6}	1067
Spherical	40	1.59×10^{-4}	0.04

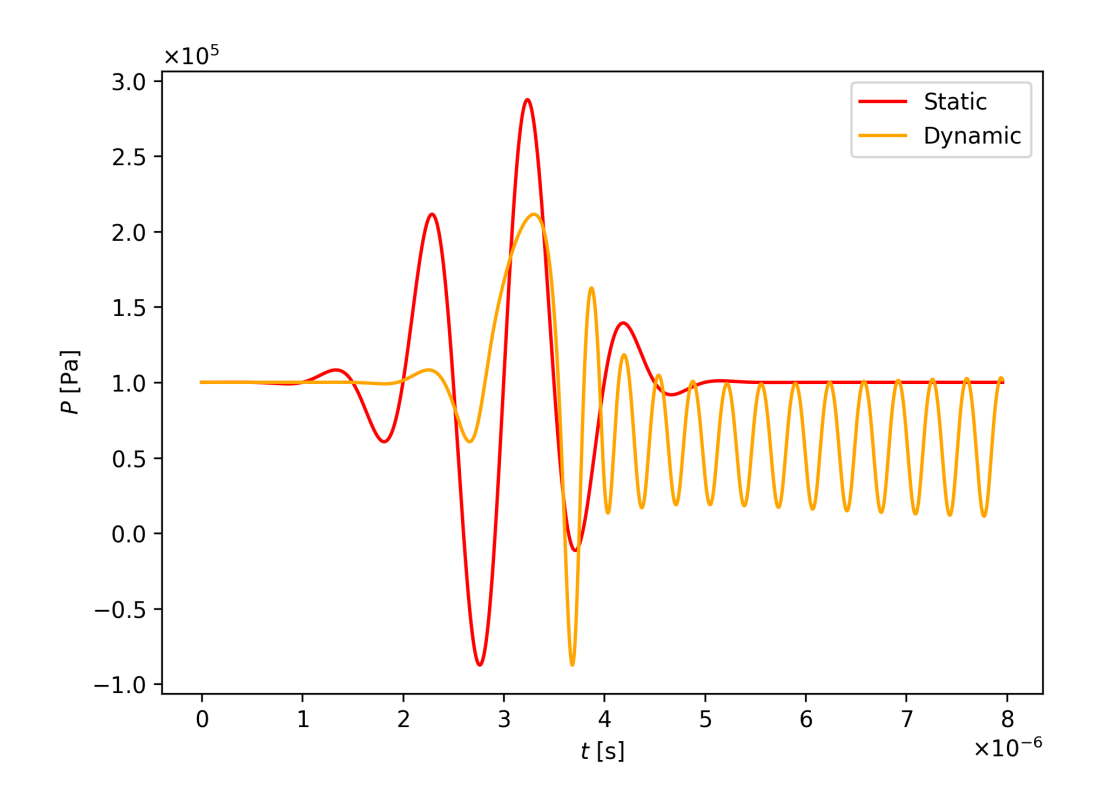


Figure 4: Comparison of the evolution of the pressure at the north pole for an EMB forced by static and dynamic Gaussian pulses with Re=6.3, De=0, $R_0=1~\mu\text{m}$, $\varepsilon=1~\text{nm}$, $\sigma=0.051~\text{N/m}$, $h=0~\mu\text{m}$, $p_A=200~\text{kPa}$ and f=1~MHz.

alent bubble radius is also reduced with the slight phase shift in oscillations before the radius converges to approximately its initial value (see Fig. 7). This is in contrast to the situation in Fig. 5. The bubble centroid undergoes several oscillations as the pressure pulse moves downwards eventually attaining a steady state approximately 0.6 μ m lower than its original position (see Fig. 8).

5. Model Predictions

The results presented in this section are concerned with the prediction of the dynamics of a bubble located near a rigid wall of infinite width along z = 0. The initial radius of the bubble is $R_0 = 1 \mu m$. The bubble is at rest at t = 0 and the radial component of the polymeric radial stress tensor

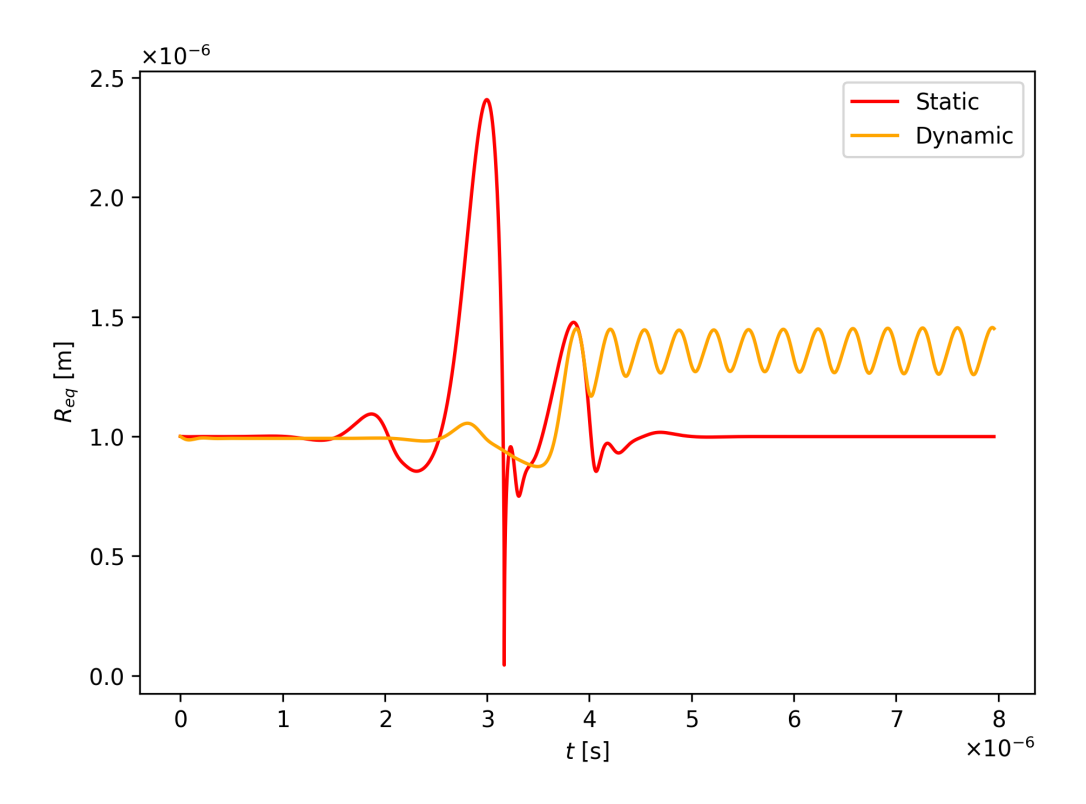


Figure 5: Comparison of the evolution of the equivalent bubble radius of an EMB forced by static and dynamic Gaussian pulses with $Re=6.3,\ De=0,\ R_0=1\ \mu\mathrm{m},\ \varepsilon=1\ \mathrm{nm},\ \sigma=0.051\ \mathrm{N/m},\ h=0\ \mu\mathrm{m},\ p_A=200\ \mathrm{kPa}$ and $f=1\ \mathrm{MHz}.$

is zero initially. Snapshots of a bubble surface in time are shown as a twodimensional cut through the bubble, due to the assumed axisymmetry. The jet velocities, $V_{\rm jet}$, shown in the figures are the velocities of the node on the bubble surface that is initially located furthest away from the wall (the north pole). The wall pressures, $P_{\rm wall}$, are calculated at the point (r, z) = (0, 0).

5.1. Effect of Shell Thickness

The effect of shell thickness on the dynamics of an EMB is investigated in the case when the stand-off distance is $h=5~\mu\mathrm{m}$. The pulse is characterised by the parameters $p_A=2$ MPa and f=2 MHz. The evolution of the bubble centroid, equivalent bubble radius and velocity of the bubble at the north pole are shown in Figs. 9a - 9c, respectively. The bubble begins to feel the influence of the pressure pulse after about 0.6 $\mu\mathrm{s}$. For a thin shell with $\varepsilon=1$

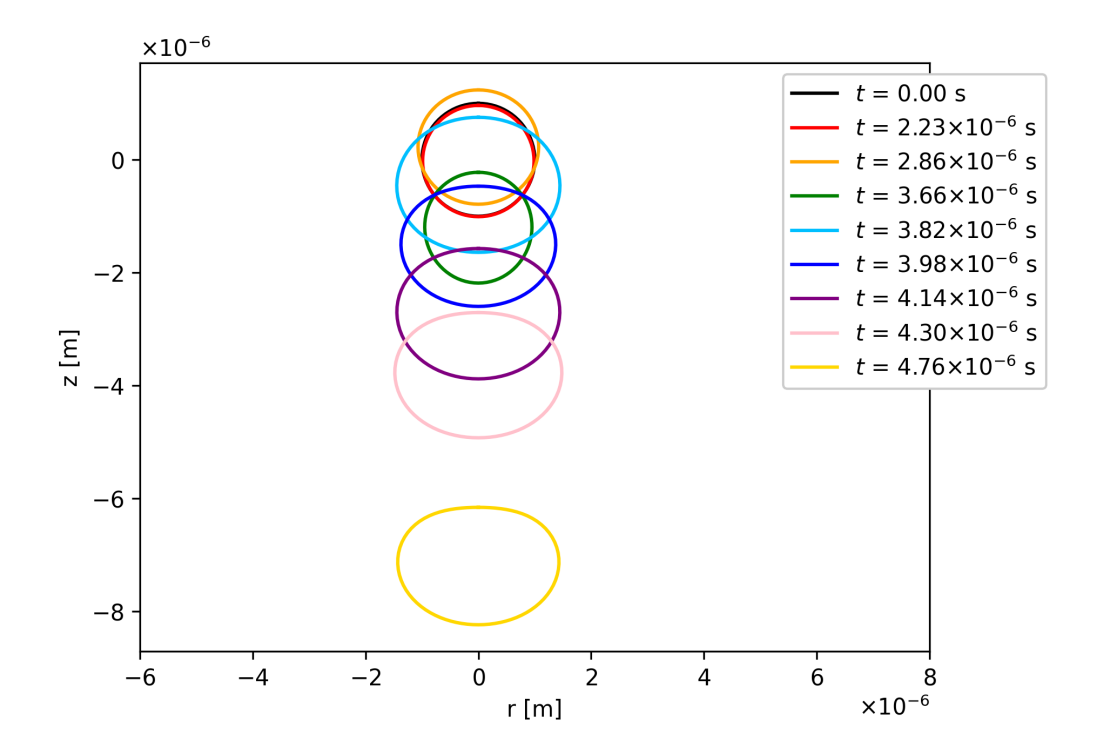


Figure 6: Evolution of bubble surfaces for an EMB forced by a Gaussian pulse with $Re=6.3,\ De=0,\ R_0=1\mu\mathrm{m},\ \varepsilon=1$ nm, $\sigma=0.051$ N/m, h=0 $\mu\mathrm{m},\ p_A=200$ kPa and f=1 MHz.

nm, the bubble centroid experiences a single oscillatory cycle before moving monotonically towards the wall until it almost touches the wall, at which point the computation stops.

Increasing the shell thickness to $\varepsilon=10$ nm, less translational movement is seen initially due to the increased resistance of the shell to deformation. At $t\approx 1.5~\mu s$, however, large growth is seen (Fig. 9b) due to the bubble entering a low pressure region of the applied pressure field with the bubble attaining a maximum equivalent bubble radius approximately three times its initial radius. The bubble is 'pushed' by this forcing pressure towards the rigid wall. As the bubble nears the wall, the jet velocity increases drastically and the bubble also begins to reduce in size, resulting in very large wall pressures shown in Figs. 9c - 9d. The pressure pulse has a minimal impact on the bubble dynamics when the shell thickness is increased further to $\varepsilon=100$ nm,

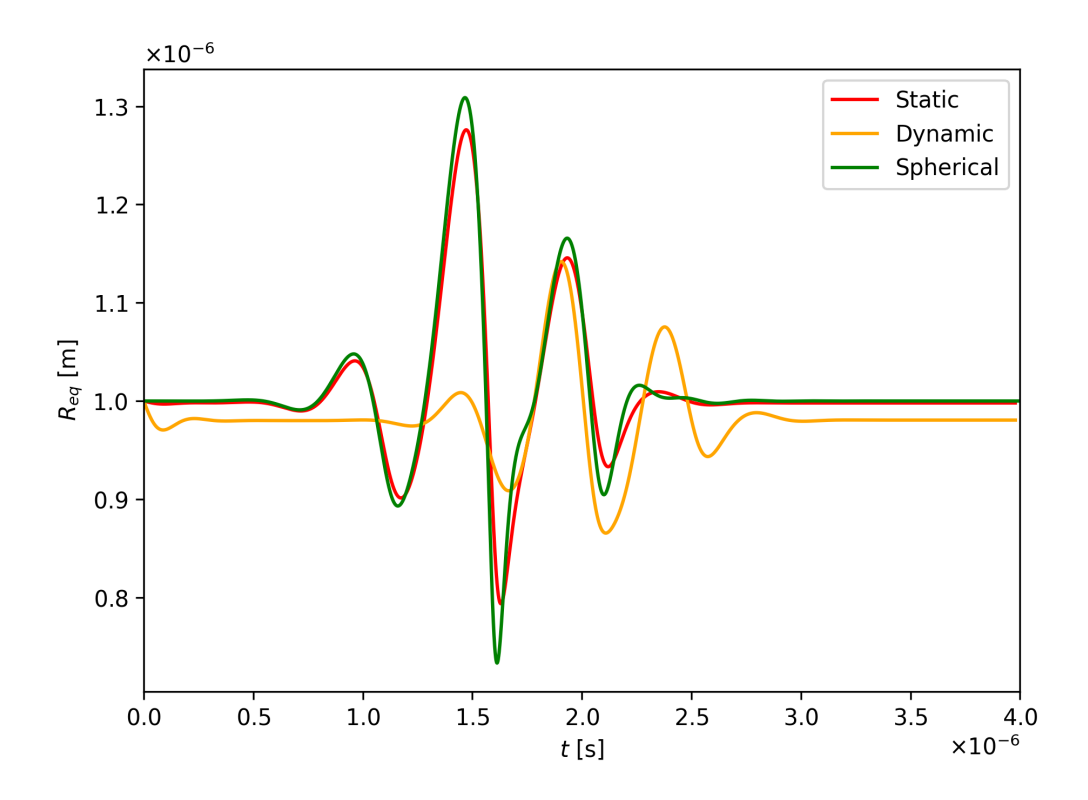


Figure 7: Comparison of the evolution of the equivalent bubble radius of an EMB forced by static and dynamic Gaussian pulses with the prediction of spherical dynamics with $Re=6.3,\ De=0,\ R_0=1\mu\mathrm{m},\ \varepsilon=1\ \mathrm{nm},\ \sigma=0.051\ \mathrm{N/m},\ h=0\ \mu\mathrm{m},\ p_A=100\ \mathrm{kPa}$ and $f=2\ \mathrm{MHz}.$

with only modest oscillation in bubble quantities and wall pressure observed at later times.

For both $\varepsilon=1$ nm and $\varepsilon=10$ nm, the simulations are terminated when the bubble surface moves to be in close proximity to the rigid wall. At this point a very thin layer of fluid is trapped between the bubble and the wall, potentially resulting in numerical instabilities. These instabilities are primarily responsible for the very large pressures that are generated at the wall as can be seen in Fig. 9d at $t\approx 1.75~\mu s$ for $\varepsilon=10$ nm. One technique that has been used to overcome these numerical difficulties is to numerically attach the bubble to the wall as described in Ni et al. [67]. The adoption of this technique into the present model, however, together with modelling contact line dynamics is left for future work.

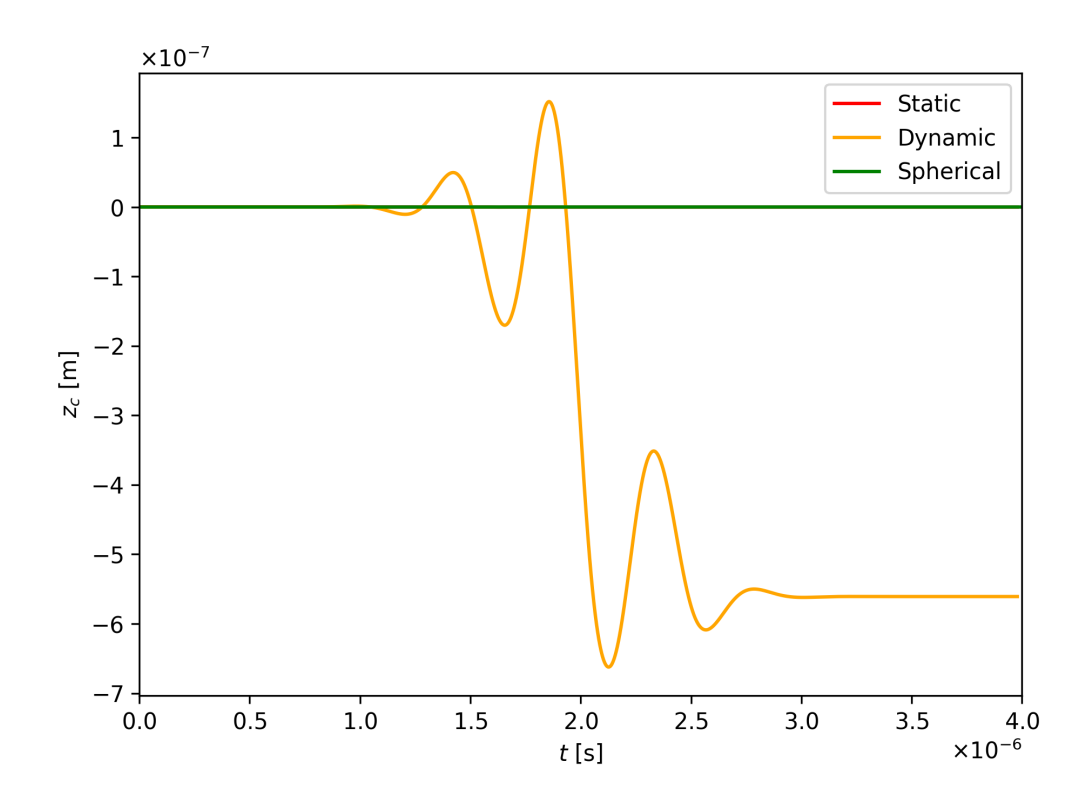


Figure 8: Comparison of the evolution of the centroid, z_c , of an EMB forced by static and dynamic Gaussian pulses with Re=6.3, De=0, $R_0=1$ μm , $\varepsilon=1$ nm, $\sigma=0.051$ N/m, h=0 μm , $p_A=100$ kPa and f=2 MHz.

Snapshots in time of the bubble surface are shown in Fig. 10 for $\varepsilon = 1, 10, 100$ nm. The bubble with $\varepsilon = 10$ nm undergoes severe deformation and rapidly moves toward the boundary, expanding as it does. It grows to an equivalent bubble radius approximately three times its initial radius over a very short period of time (Fig. 10b). Clearly, this intermediate value of $\varepsilon = 10$ nm elicits the most significant dynamical response, unlike that of $\varepsilon = 100$ nm, for example, which seems to impose an overly restrictive bubble coating, likely at the limit for which the thin-shell assumption made in Eqn. (19) is valid. Snapshots of the velocity field are shown in Fig. 11 for $\varepsilon = 1$ nm at $1.38 \times 10^{-6} s$ and $\varepsilon = 10$ nm at $1.74 \times 10^{-6} s$. The velocity vector is normalized to highlight the direction of the fluid motion. Similarly to the observation of a jet in Fig. 9c, at $\varepsilon = 1, 10$ nm, the beginnings of a jet are observed to form above the bubble, generating a flow that collapses the

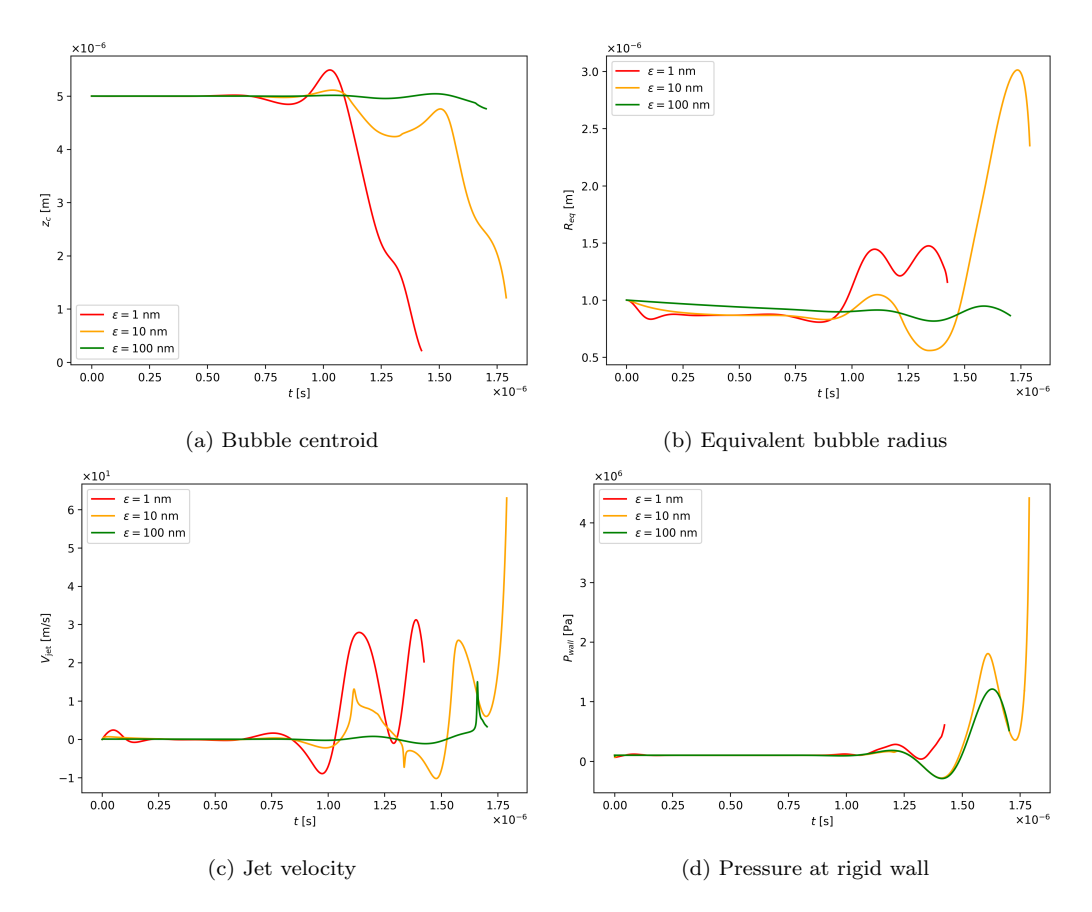


Figure 9: Influence on shell thickness on the evolution of bubble dynamics for Re=6.3, De=0, $R_0=1$ μm , $\sigma=0.051$ N/m, h=5 μm , $p_A=2$ MPa, f=2 MHz and $\varepsilon=1$ nm, 10 nm, 100 nm.

bubble.

5.2. Effect of Fluid Viscoelasticity

The viscoelasticity of the fluid is modelled using the Oldroyd B model. The constitutive equation (24) is an evolution equation for the polymer contribution to the stress. This is solved simultaneously with Eqns. (19) - (20) to update the system in time. In Figs. 12 - 16 and Figs. 17 - 18, the effects of changing fluid viscosity are shown for small (De = 0.5) and large (De = 10) Deborah numbers, respectively. Two different shell thicknesses ($\varepsilon = 1$ nm and $\varepsilon = 10$ nm) are also considered for De = 0.5.

For De = 0.5 with $\varepsilon = 1$ nm, as the Reynolds number is increased

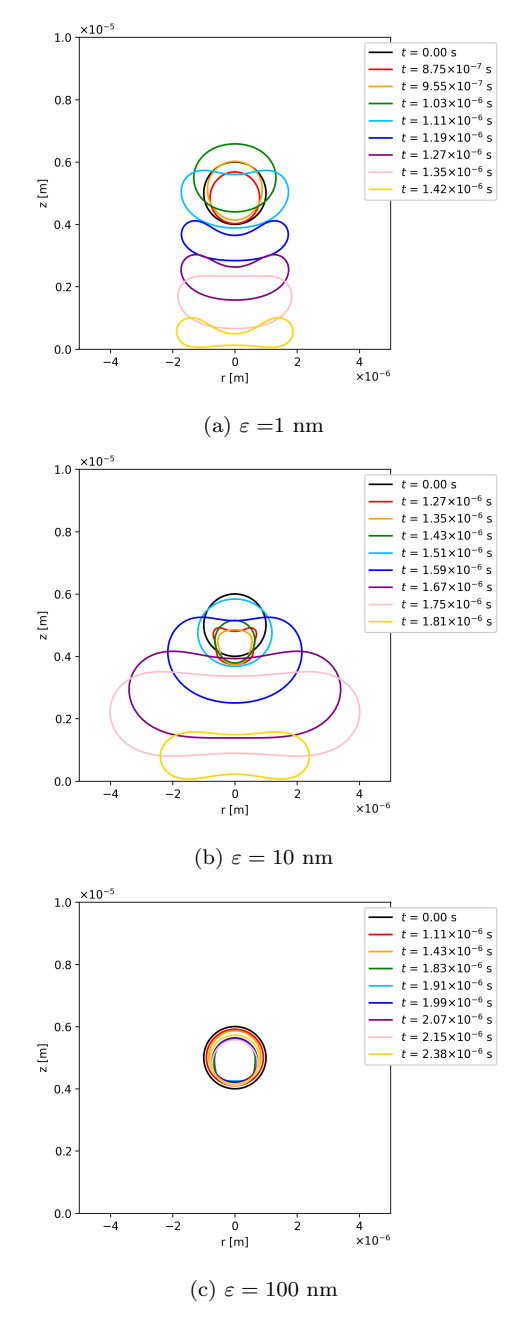


Figure 10: Snapshots of the bubble surface for $Re=6.3,\,De=0,\,R_0=1$ µm, $\sigma=0.051$ N/m, h=5 µm, $p_A=2$ MPa , f=2 MHz and $\varepsilon=1$ nm, 10 nm, 100 nm.

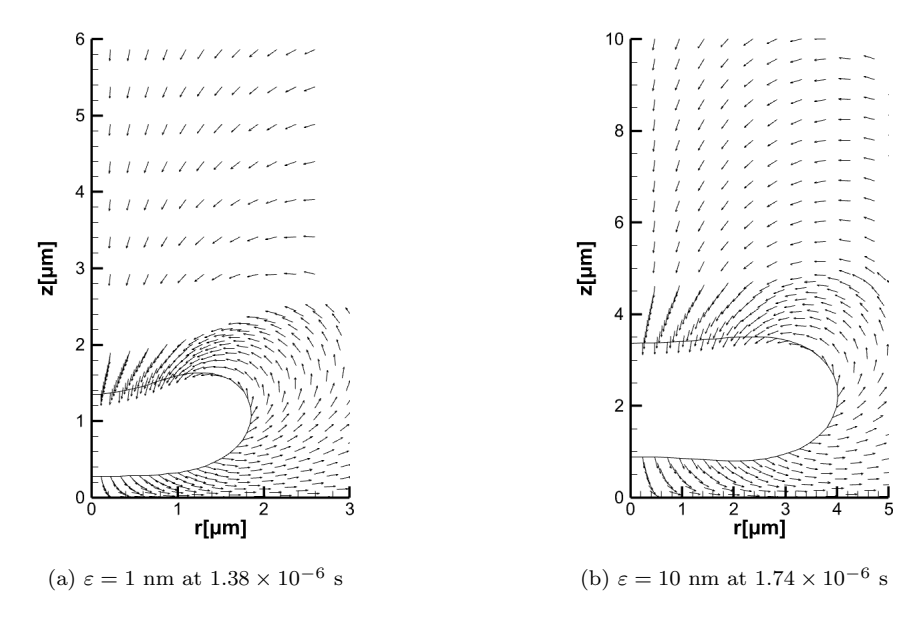


Figure 11: Snapshots of the normalized velocity field for $Re=6.3,\ De=0,\ R_0=1\ \mu\text{m},\ \sigma=0.051\ \text{N/m},\ h=5\ \mu\text{m},\ p_A=2\ \text{MPa}$, $f=2\ \text{MHz}$: (a) $\varepsilon=1\ \text{nm}$, (b) $\varepsilon=10\ \text{nm}$.

(corresponding to a lower viscosity) an earlier response to the acoustic forcing is observed. This is evidenced by the earlier translational movement of the bubble towards the boundary (which occurs at near uniform speed, regardless of Re, see Fig. 12a), earlier (initial) bubble growth (Fig. 13a) and earlier increase in jet velocities (Fig. 14a). For Re = 1 the bubble grows rapidly after around $t = 1\mu s$ with a violent collapse phase occurring at $t \approx 1.8$ μ s (see Fig. 13a). Complete bubble collapse does not occur within the duration of the computations in these cases due to the onset of numerical instabilities. These can occur when the bubble moves so close to the rigid wall that there is only a very thin layer of fluid between. When this occurs the computations are terminated before a possible liquid jet (and transition to toroidal form) forms. The corresponding rigid wall pressures attained seem to be largely independent of Re at least initially (see Fig. 15a), with differences in wall pressure only evident in the final stages of near-wall bubble motion. Snapshots of the bubble surface over time for Re = 1 are shown in Fig. 16 for both shell thickness ($\varepsilon = 1$ nm and $\varepsilon = 10$ nm). Interestingly, increasing the shell thickness appears to reduce dependence on Reynolds number for all flow quantities considered. In each case (Figs. 12b- 14b, with $\varepsilon = 10$ nm), very similar results are obtained regardless of Reynolds number value

up to $t \approx 1 \ \mu s$. At this shell thickness, shell response clearly dominates over hydrodynamical viscous forces.

For the same range of Reynolds numbers, the bubble dynamics are shown in Fig. 17 for the (higher-elasticity) case De = 10. Note only one shell thickness ($\varepsilon = 1$ nm) is considered. On increasing De, there remains a similarity in the behaviour across Reynolds numbers to the previous case (De = 0.5). Evidently, despite elevated levels of fluid elasticity, dynamics are still dominated by viscous and shell effects. For example, as seen for De =0.5, the equivalent bubble radius for Re = 1 becomes four times as large as its initial value during the simulation (see Fig. 17b at $t \approx 1.5 \ \mu s$). Similarly, rigid wall pressures are also notably larger for the Re = 1 case, compared to Re = 4,10 (Fig. 17d) where, eventually, a near-wall numerical instability is initiated, indicated by the prediction of negative pressures. Bubble centroid movement is also broadly similar to the De = 0.5 case from Fig. 12a: for De = 10 when Re = 1 (Fig. 17a), the bubble remains in a low pressure region of the pulse for longer since there is less translational movement, until $t \approx 1.1 \ \mu s$. Subsequently, the bubble translates relatively quickly toward the wall (whilst growing and flattening) before reaching the wall, decreasing slightly in size, and creating the large pressures shown in Fig. 17d. Upon making contact with the wall the simulation is terminated. Figure 18 shows this evolution of the bubble surface at various times (Re = 1, De = 10).

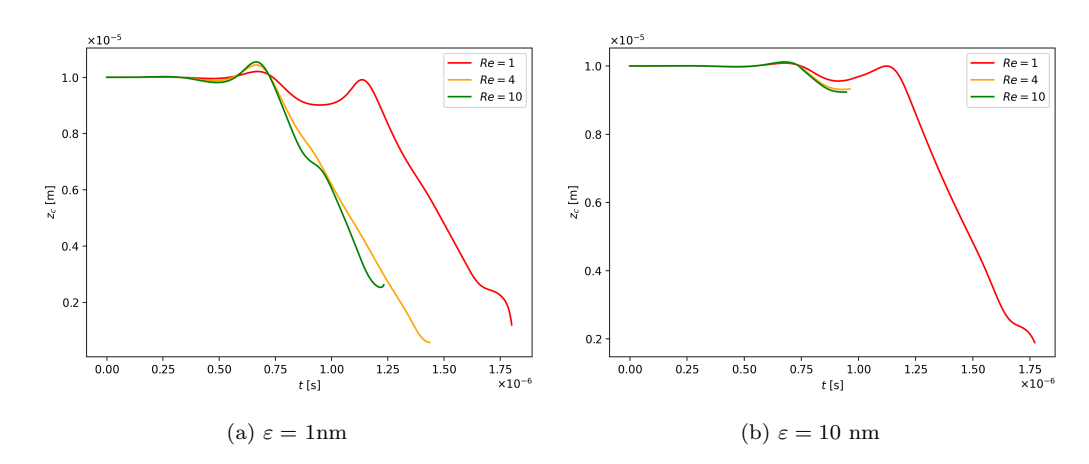


Figure 12: Comparison of the evolution of the bubble centroid position on shell thickness for $De=0.5,\ R_0=1\ \mu\mathrm{m},\ \varepsilon=1\ \mathrm{nm},\ 10\ \mathrm{nm},\ \sigma=0.051\ \mathrm{N/m},\ h=10\ \mu\mathrm{m},\ p_A=2\ \mathrm{MPa}$, $f=2\ \mathrm{MHz}$ and Re=1,4,10.

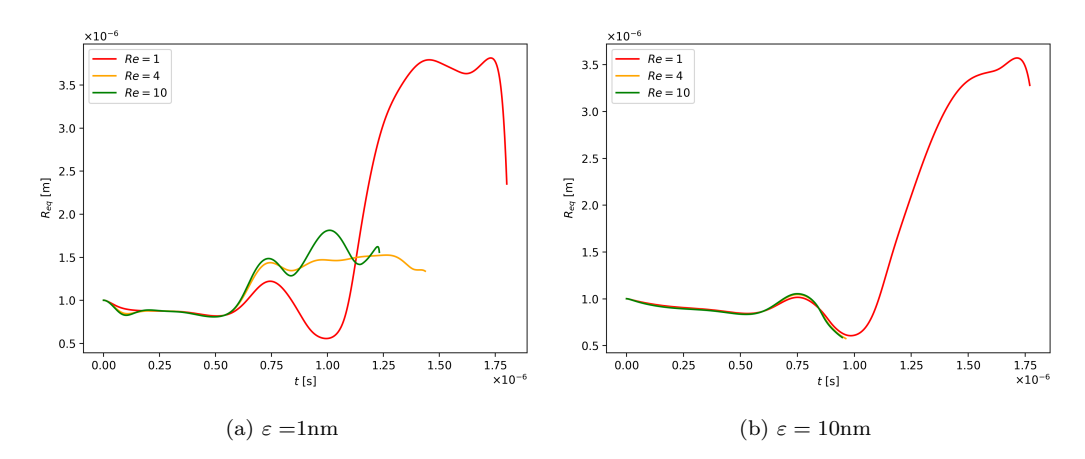


Figure 13: Comparison of the evolution of the equivalent bubble radius on shell thickness for $De=0.5,\ R_0=1\mu\mathrm{m},\ \varepsilon=1$ nm, 10 nm, $\sigma=0.051$ N/m, h=10 $\mu\mathrm{m},\ p_A=2$ MPa, f=2 MHz and Re=1,4,10.

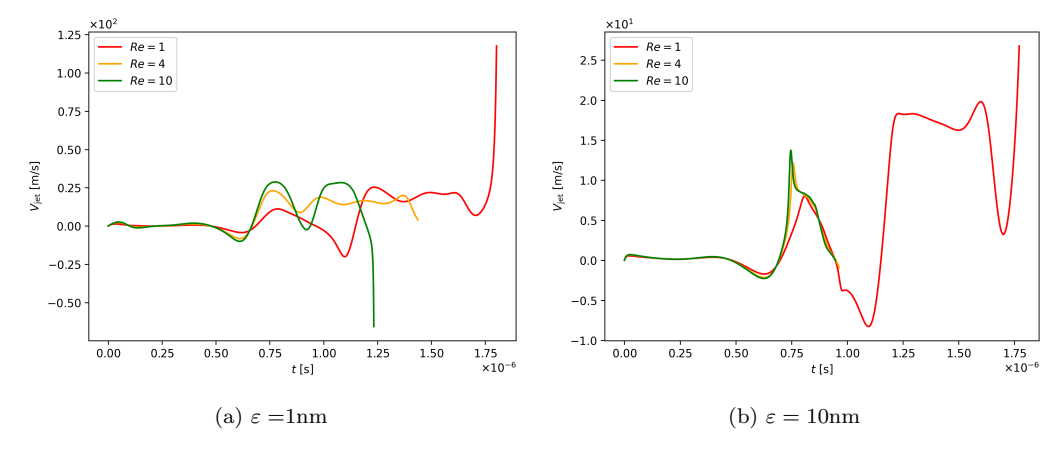


Figure 14: Evolution of the jet velocity for parameters $De=0.5,~R_0=1~\mu\mathrm{m},~\varepsilon=1~\mathrm{nm},$ 10 nm, $\sigma=0.051~\mathrm{N/m},~h=10~\mu\mathrm{m},~p_A=2~\mathrm{MPa}$, $f=2~\mathrm{MHz}$ and Re=1,4,10.

5.3. Effect of Pulse Frequency

For a spherical EMB, the effects of pulse frequency were investigated theoretically and experimentally by Wu et al. [66]. The authors observed that lower-frequency ultrasound induced more vigorous oscillations under similar acoustic pressures. The effects of changing the pulse frequency on a non-spherical EMB are shown in Figs. 19 - 22 for a bubble in an Oldroyd-B fluid with Re = 1, De = 0.5, for two different shell thicknesses ($\varepsilon = 1, 10$ nm). For $\varepsilon = 1$ nm, the response to the pulse is larger for a pulse frequency

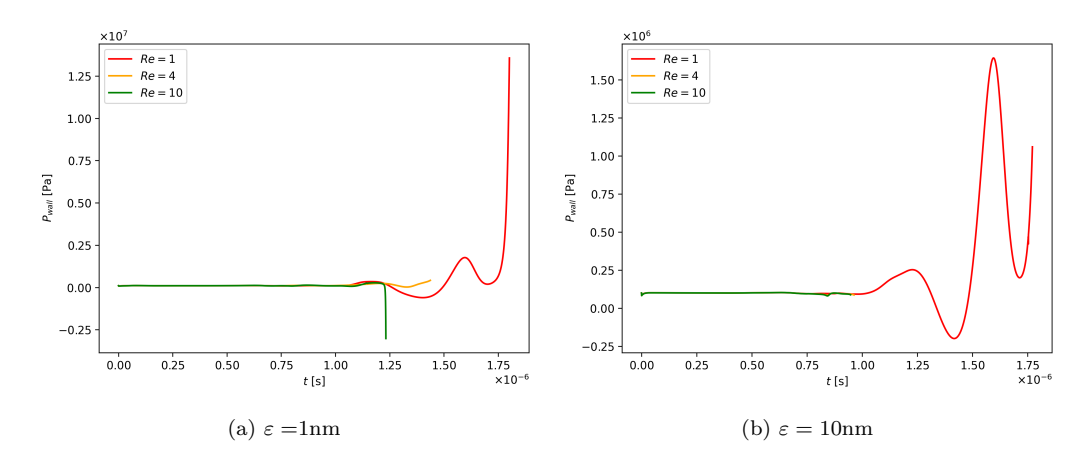


Figure 15: Evolution of the pressure at the rigid wall for parameters $De=0.5,\,R_0=1\mu\mathrm{m},\,\varepsilon=1$ nm, 10 nm, $\sigma=0.051$ N/m, h=10 $\mu\mathrm{m},\,p_A=2$ MPa , f=2 MHz and Re=1,4,10.

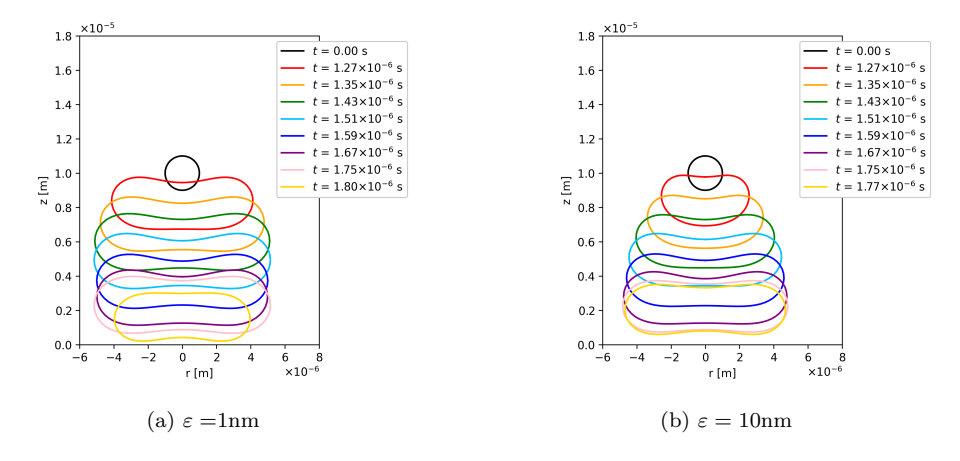


Figure 16: Dependence of shell thickness on snapshots of the bubble surface in the first singly-connected phase for parameters $Re=1, De=0.5, R_0=1$ µm, $\varepsilon=1$ nm, 10nm, $\sigma=0.051$ N/m, h=10 µm, $p_A=2$ MPa and f=2 MHz.

of f=2 MHz than for most other frequencies, but responses to f=4 MHz and f=5 MHz are quite significant at early times (before around 1 μ s). This can be seen by noting the rapid increase in bubble equivalent radius (and subsequently larger bubble volume attained, Fig. 19a). When f=2 MHz the oscillating pressure pulse causes the bubble to shrink slightly after its initial growth at $t\approx 1.75~\mu$ s. At the lower frequencies (f=1,2,4 MHz) there is also larger translational movement (Fig. 20). For $\varepsilon=10$ nm, the greatest jet velocities (Fig. 21) and wall pressures (Fig. 22) are

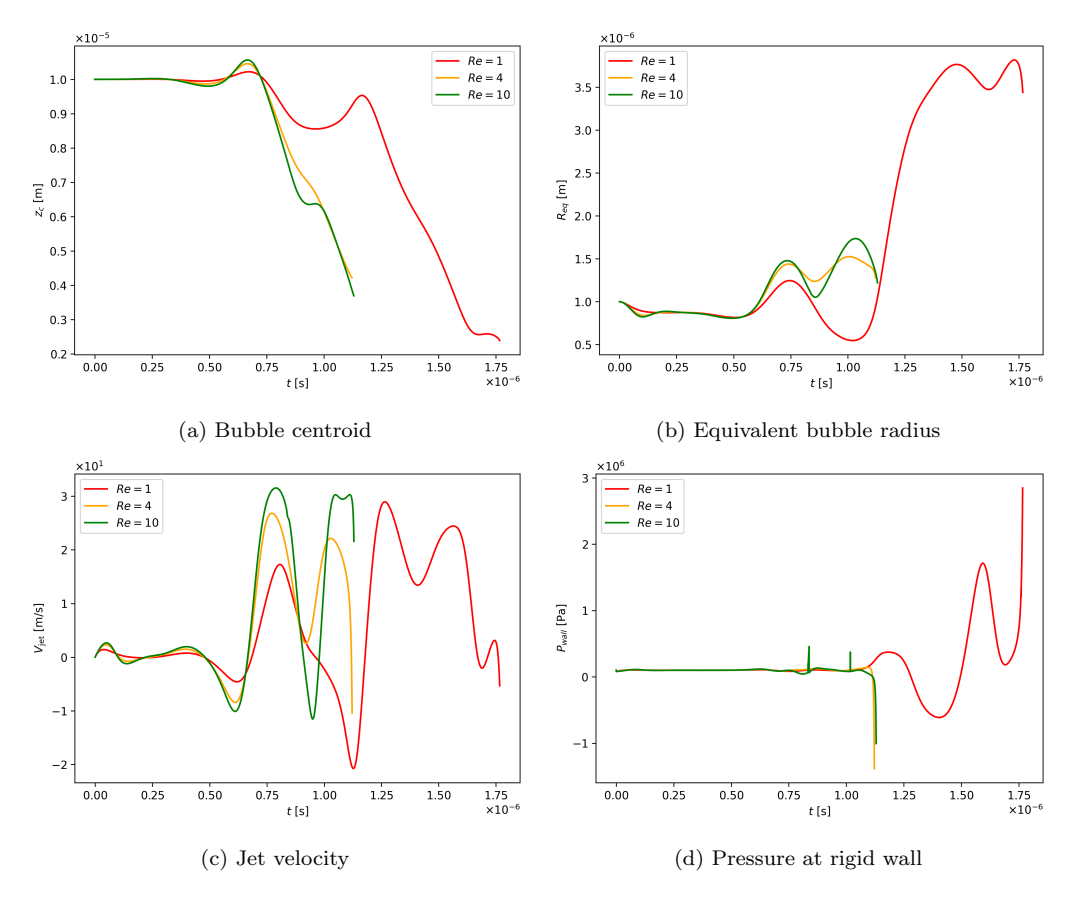


Figure 17: Influence of Reynolds number on the evolution of bubble dynamics for De=10, $R_0=1~\mu\text{m},~\varepsilon=1\text{nm},~h=10~\mu\text{m},~\sigma=0.051~\text{Nm},~p_A=2~\text{MPa}$ and f=2~MHz.

also observed when f=2 MHz (although for these flow measures there is no clearly dominant frequency when $\varepsilon=1$ nm). Note that for the shell model used here the resonant frequency of the bubble, f_0 , can be determined analytically (see, for example, [15]) to be

$$f_0 = \frac{1}{2\pi R_0} \sqrt{\frac{1}{\rho} \left(3\kappa p_0 + 12\chi_{sh} \frac{\varepsilon}{R_0} + \frac{2\sigma}{R_0} (3\kappa - 1) \right)},\tag{38}$$

which for the chosen parameters yields a resonant frequency value of approximately 2.8 MHz - close to 2MHz and within the range of frequencies (1-4 MHz) that tend to elicit the largest responses here. When f = 1 MHz, the bubble is pushed by the pulse towards the rigid wall while remaining at

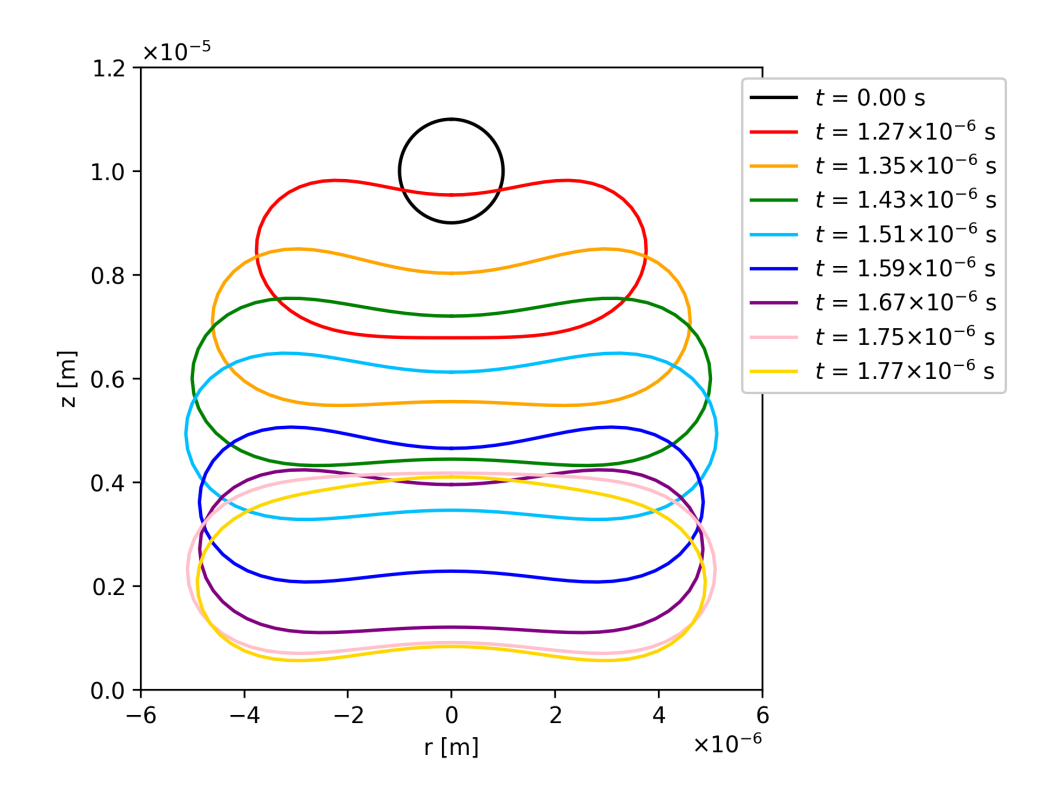


Figure 18: Snapshots of the bubble surface for Re=1, De=10, $R_0=1~\mu\text{m}$, $\varepsilon=1~\text{nm}$, $\sigma=0.051~\text{Nm}$, $h=10~\mu\text{m}$, $p_A=2~\text{MPa}$ and f=2~MHz.

roughly the same size (see Figs. 19 and 20). The simulation is terminated when the bubble becomes too close to the wall. Increasing the shell thickness to $\varepsilon = 10$ nm (Figs. 19b - 22b) does not markedly change the qualitative behaviour in this instance: lower frequencies still tend to produce the most significant response.

Snapshots of the bubble surface for f=4 MHz are shown in Fig. 23 for the two different shell thicknesses. When $\varepsilon=1$ nm the bubble oscillates until $t\approx 1~\mu s$ before attaching to the wall in a pear-like shape. The computations are terminated at this point. For $\varepsilon=10$ nm, bubble dynamics is much more subdued and constrained by the increased shell thickness, with low amplitude, near spherical oscillation and minimal translational movement observed over approximately the same time duration.

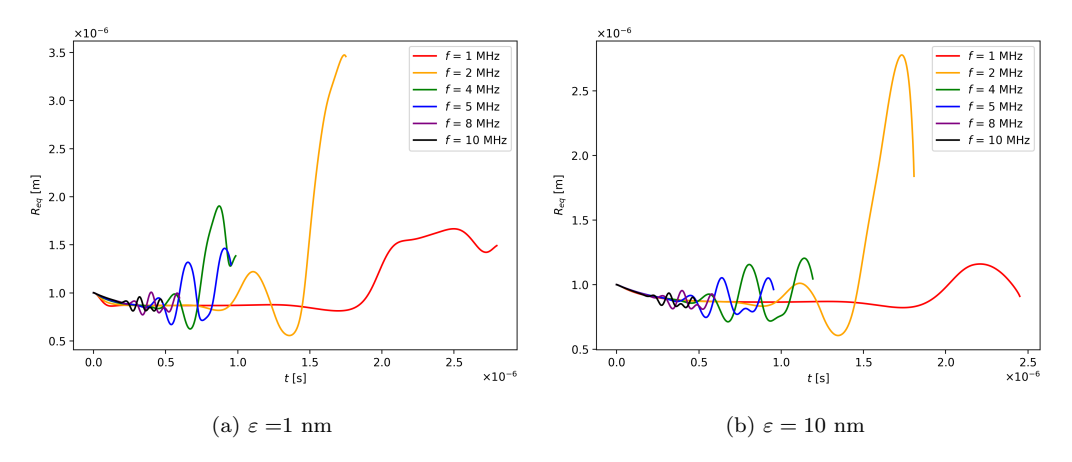


Figure 19: Dependence of the evolution of the equivalent bubble radius on pulse frequency for $Re=1,\,De=0.5,\,R_0=1$ $\mu\text{m},\,\varepsilon=1$ nm, 10nm, $\sigma=0.051$ N/m, h=5 μm and $p_A=2$ MPa: (a) $\varepsilon=1$ nm, (b) $\varepsilon=10$ nm

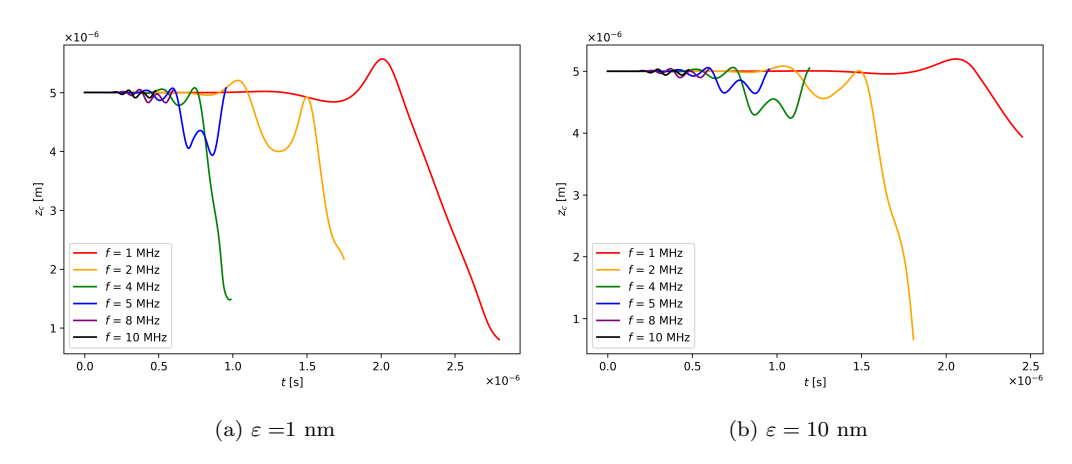


Figure 20: Dependence of the evolution of bubble centroid position on pulse frequency for $Re=1, De=0.5, R_0=1 \ \mu\text{m}, \sigma=0.051 \ \text{N/m}, h=5 \ \mu\text{m}$ and $p_A=2 \ \text{MPa}$: (a) $\varepsilon=1 \ \text{nm}$, (b) $\varepsilon=10 \ \text{nm}$.

5.4. Effect of Pulse Strength

So far in this paper, numerical predictions of bubble dynamics have been presented for a pressure amplitude of $p_A = 2$ MPa since this is a typical value for pulse strength used in sonoporation. In ultrasound contrast imaging, however, the pressure amplitudes are typically of the order of 100 kPa. In Figs. 24, results are presented for a fixed pulse frequency f = 2MHz and a range of pressure amplitudes: $p_A = 200$ kPa, 400 kPa, 2 MPa.

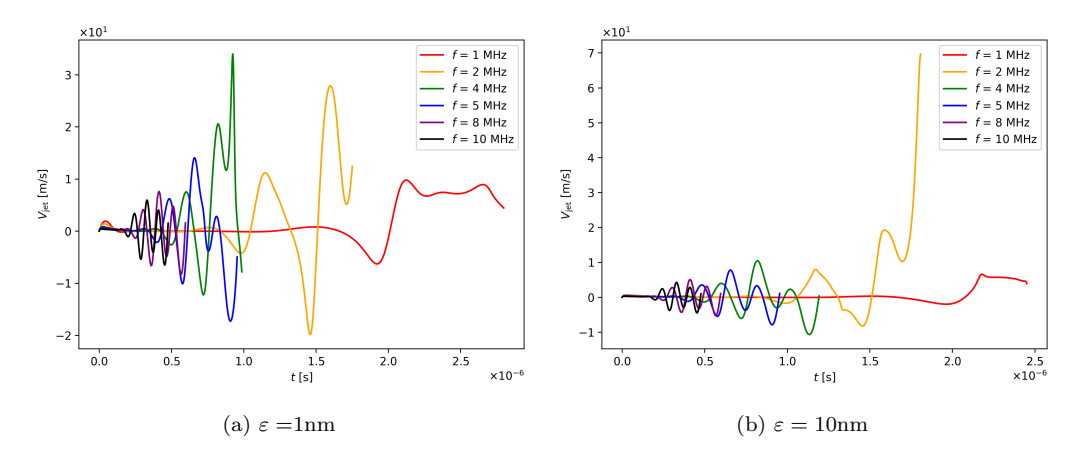


Figure 21: Dependence of jet velocity on pulse frequency for Re=1, De=0.5, $R_0=1$ μm , $\sigma=0.051$ N/m, h=5 μm and $p_A=2$ MPa: (a) $\varepsilon=1$ nm, (b) $\varepsilon=10$ nm.

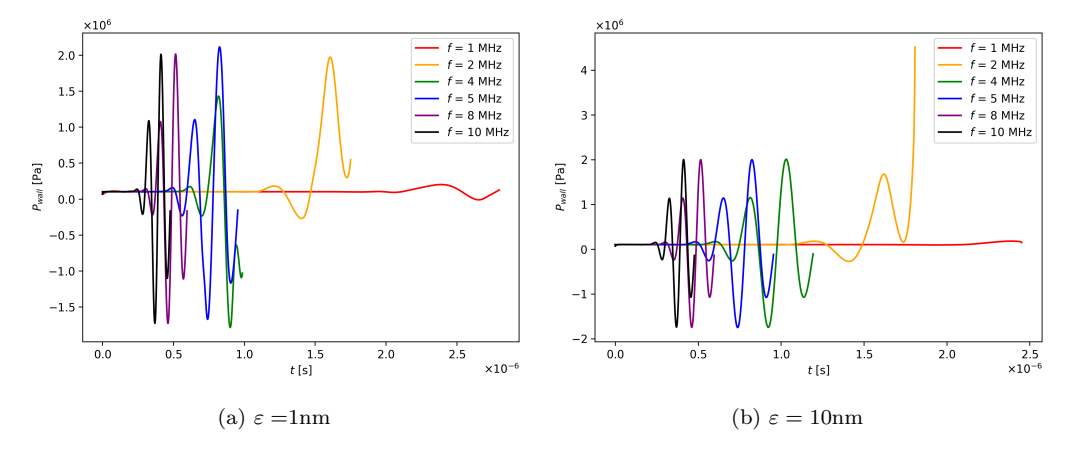
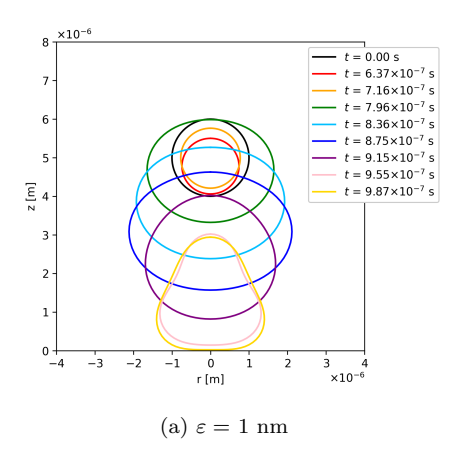


Figure 22: Dependence of pressure at the rigid wall on pulse frequency for Re=1, $De=0.5,\ R_0=1\ \mu\text{m},\ \sigma=0.051\ \text{N/m},\ h=5\ \mu\text{m}$ and $p_A=2\ \text{MPa}$: (a) $\varepsilon=1\ \text{nm}$, (b) $\varepsilon=10\ \text{nm}$.

The majority of EMBs have been shown [68] to undergo stable, harmonic oscillations for pressure amplitudes in the range 50 kPa - 200 kPa, with higher amplitudes potentially leading to spontaneous acoustic emissions and bubble fragmentation. The numerical predictions presented here agree well qualitatively with these experimental findings since in the lowest amplitude cases considered for which $p_A = 200$ kPa and $p_A = 400$ kPa, the bubble undergoes stable oscillations about its initial volume and position. In the case for which $p_A = 2$ MPa, the bubble grows rapidly as it is pushed towards



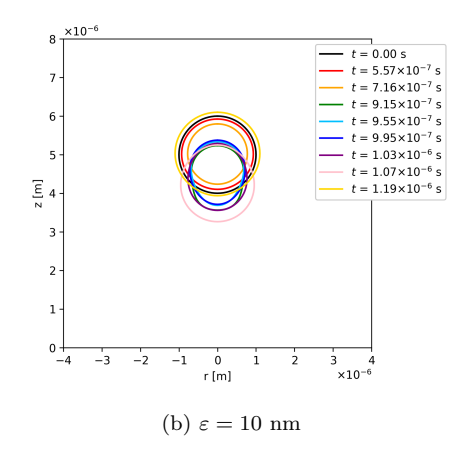


Figure 23: Dependence of shell thickness on snapshots of the bubble surface for Re=1, De=0.5, $R_0=1~\mu\text{m}$, $\sigma=0.051~\text{N/m}$, $h=5~\mu\text{m}$, $p_A=2~\text{MPa}$ and f=4~MHz: (a) $\varepsilon=1~\text{nm}$, (b) $\varepsilon=10~\text{nm}$.

the boundary, with significant jet velocities and wall pressures predicted. This case has been discussed earlier (see Figs. 12 - 15).

5.5. Effect of Surface Tension

The influence of surface tension on the evolution of bubble dynamics is shown in Fig. 25 for Re=1, De=0.5, $h=10~\mu\text{m}$, $\varepsilon=1~\text{nm}$, $p_A=2~\text{MPa}$, f=2~MHz. In particular we have increased and decreased the default value of σ used in this paper by a factor of two. Changing the value of σ in this way has negligible impact on bubble dynamics. Clearly, Young-Laplace surface tension is not as important as the properties of the shell in terms of the dynamics.

5.6. Effect of Stand-off Distance

The influence of initial stand-off distance, h, on the evolution of bubble dynamics is shown in Fig. 26 for Re=1, De=0.5, $\varepsilon=1$ nm, $p_A=2$ MPa, f=2 MHz, $\sigma=0.051$ N/m. In particular, we present results for h=5, 10, 15 μ m. The evolution of bubble centroid, equivalent bubble radius and jet velocity shown in Figs. 26a - 26c exhibit almost linear translational behaviour with respect to h. The larger the value of h the earlier the bubble begins to respond to the pressure pulse in terms of the motion of the bubble centroid towards the rigid wall and the onset of bubble expansion. The jet velocity experiences similar behaviour before increasing substantially at about t=1.8

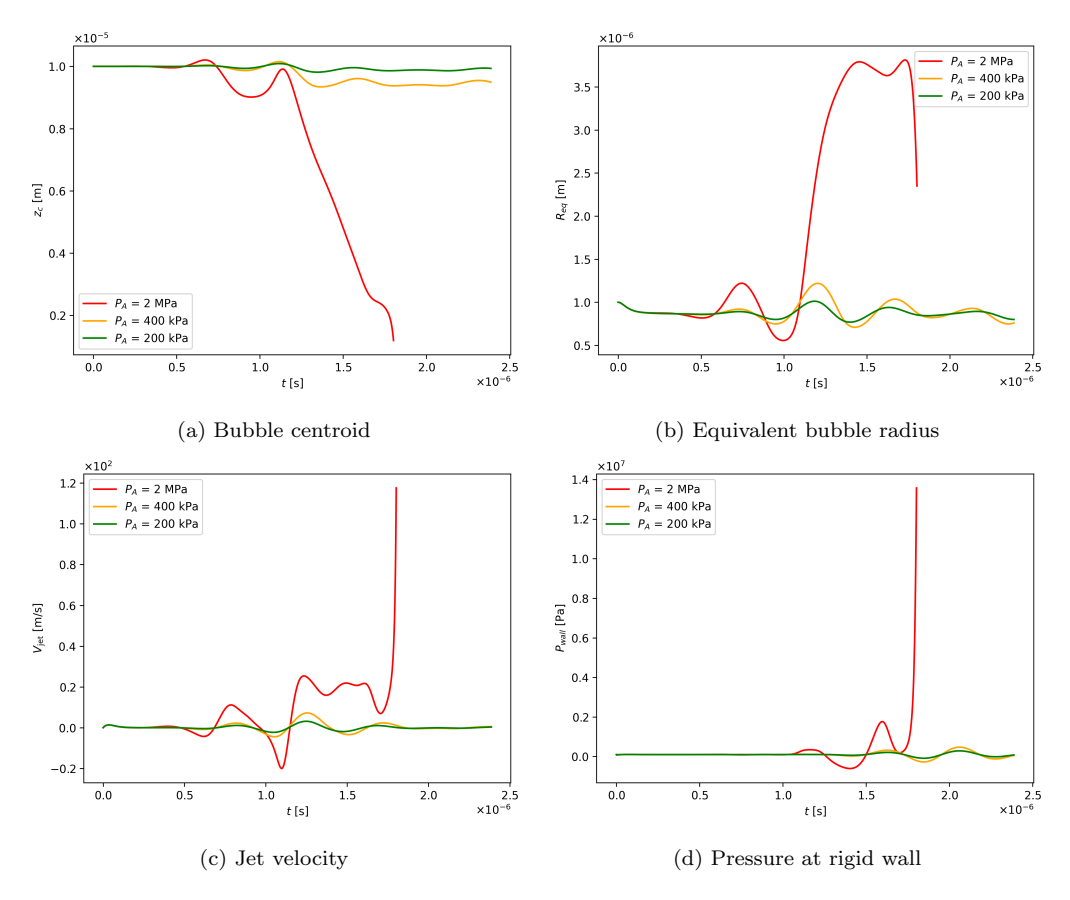


Figure 24: Influence of pulse strength on the evolution of bubble dynamics for Re=1, De=0.5, $R_0=1~\mu\text{m}$, $\varepsilon=1~\text{nm}$, $h=10~\mu\text{m}$, f=2~MHz and $\sigma=0.051~\text{N/m}$.

 μ s (approximately the point at which the bubble reaches the rigid wall). This increase is accompanied by a sharp collapse in bubble volume and a sharp increase in the pressure at the rigid wall. Fig. 26 shows that although the value of h influences the transient behaviour of bubble dynamics, the terminal behaviour of the bubble including the time at which this occurs is independent of h.

6. Conclusions

In this paper an encapsulated microbubble in a viscoelastic fluid forced by a pressure field is modelled using a modified boundary element method. Viscous and interfacial terms are included to account for the influence of the

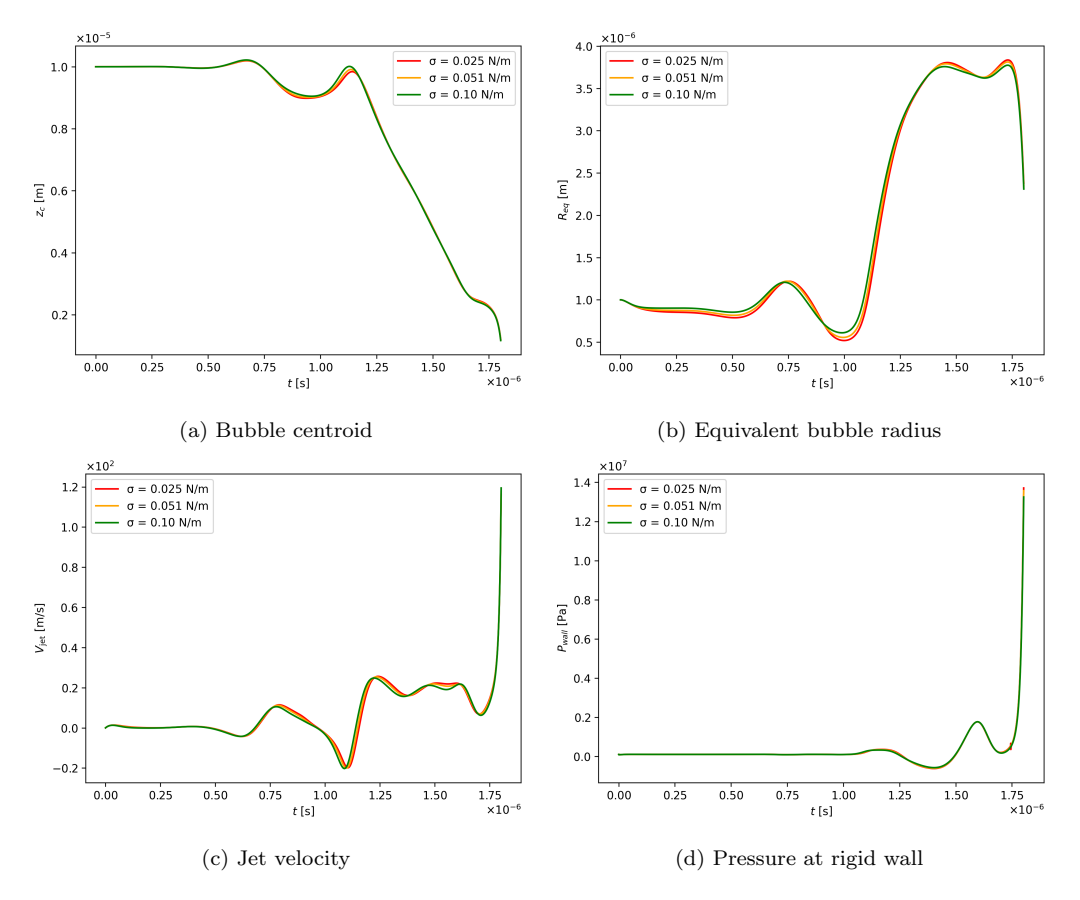


Figure 25: Influence of surface tension coefficient on the evolution of bubble dynamics for Re = 1, De = 0.5, $R_0 = 1$ μ m, $\varepsilon = 1$ nm, h = 10 μ m, $p_A = 2$ MPa and f = 2 MHz.

shell using an extension of the spherical model developed by Church [8].

For a bubble in an infinite fluid, the non-spherical BEM simulations produce significantly different results to the spherical model. This is due to the translational movement of the bubble in the direction of the pressure field and non-spherical deviations. These mechanisms (which are not able to be predicted by the spherical model) are significant even at relatively low pressure amplitudes.

We have shown that a large shell thickness reduces the translational movement and jet velocities of the EMB. This is expected since a thicker shell provides more stability making the bubble more resistant to deformation.

The effect of changing fluid viscoelasticity is also investigated by altering the Reynolds and Deborah numbers. Typically, a decrease in fluid viscosity

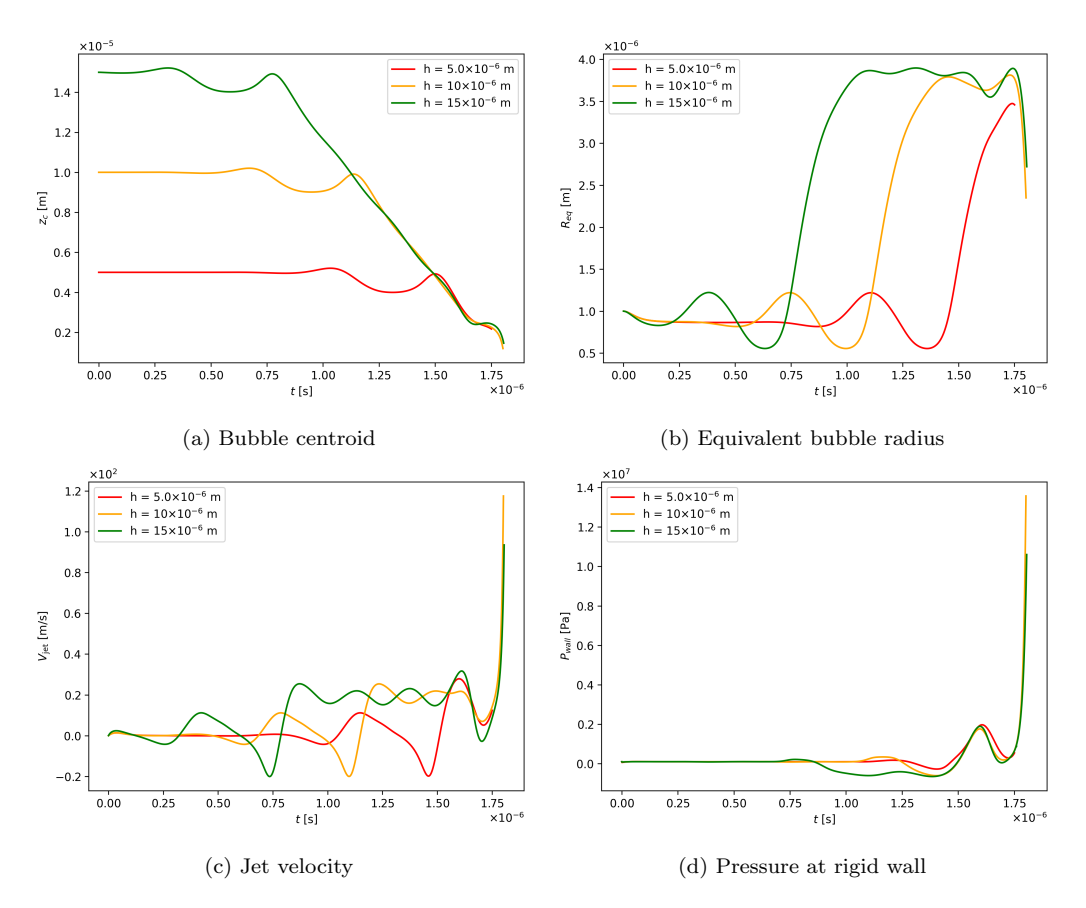


Figure 26: Influence of stand-off distance on the evolution of bubble dynamics for Re=1, $De=0.5, R_0=1~\mu\text{m}, \varepsilon=1~\text{nm}, \sigma=0.051~\text{N/m}, p_A=2~\text{MPa}$ and f=2~MHz.

results in an earlier response to the acoustic forcing. At lower Reynolds numbers, the stabilising effect of viscosity, in combination with elastic effects, is such that significant growth can be observed over a longer time duration and interaction with the pressure pulse. Importantly, for increased shell thicknesses, results appear largely independent of viscosity (at least for early times) as shell surface forces dominate over viscous/hydrodynamical. Similar bubble behaviour is observed at larger flow elasticities, with any potential dominance of elasticity mitigated by the bubble shell for the parameters considered.

The effects of the properties of the acoustic pulse, viz. pulse frequency (f) and strength (p_A) , on bubble dynamics have also been considered. Generally, a larger response is seen for lower frequencies (especially around 2MHz).

A higher pulse strength naturally leads to higher jet velocities and more distortion of the bubble, and it is found that the EMB, on approaching the wall, can become quite distorted with the potential to disintegrate. Indeed, further studies are required particularly when the bubble moves to be in close proximity to the wall. In this case the numerical method will need to be modified to model the attachment of the bubble to the wall so that the simulations can be continued to obtain an improved understanding of EMB dynamics, including continuation of any bubble jets and potential formation of toroidal bubbles (which have not been observed in any cases in this work).

Finally, the influence of surface tension (via the Young-Laplace law) and bubble-wall stand-off distance are investigated. The role of surface tension is negligible in the presence of viscoelasticity and the bubble shell, suggesting this term may be neglected for future studies. Similarly, the stand-off distance has little effect on the overall dynamics and terminal behaviour of the bubble, and acts primarily to shift the start time for bubble-pulse interaction.

In this paper the effects of heat and mass transfer have been neglected, and, as mentioned, extending the model to allow for bubble-wall attachment dynamics remains key. Nevertheless, useful quantitative insights have been obtained for realistic ultrasound and biological fluid parameters, with the stabilising effect of the bubble shell clear and apparently dominant over fluid rheology. Future work will include a bubble-wall attachment capability, as well as the modelling ideas of Szeri et al. [33] to model heat and mass transfer for EMBs forced by ultrasound in a viscoelastic fluid.

In this paper we have also assumed that the viscoelastic shell properties remain constant with frequency. However, attenuation experiments [69] have suggested that the shell stiffness and viscosity of phospholipid EMBs can be frequency dependent at ultrasound frequencies of 10 MHz and above. These shell properties play a crucial role in determining the linear and nonlinear response to ultrasound and so it will be important to model this behaviour in the future when studying applications of ultrsound that utilize frequencies in this range.

Acknowledgements

This research was partly supported through a PhD studentship for MJW funded by Cardiff School of Mathematics. This work was supported by JSPS KAKENHI Grant Number JP23K03673 and JP20K04285. HF would like to

acknowledge funding from the NITech Funding Program for Researcher Overseas Visits. We would also like to thank the reviewers for their constructive comments which have helped to improve this paper.

References

- [1] D. Cosgrove, Ultrasound contrast agents: An overview, Eur. J. Radiol. 60 (2006) 324–330.
- [2] P. N. T. Wells, Ultrasound imaging, Phys. Med. Biol. 51 (2006) R83– R89.
- [3] A. A. Doinikov, S. Zhao, P. A. Dayton, Modeling of the acoustic response from contrast agent microbubbles near a rigid wall, Ultrasonics 49 (2) (2009) 195–201.
- [4] S. Bao, B. D. Thrall, D. L. Miller, Transfection of a reporter plasmid into cultured cells by sonoporation in vitro, Ultrasound Med. Biol. 23 (6) (1997) 953–959.
- [5] D. L. Miller, S. V. Pislaru, J. F. Greenleaf, Sonoporation: Mechanical DNA delivery by ultrasonic cavitation, Somat. Cell. Molec. Gen. 27 (2002) 115–134.
- [6] A. Bouakaz, J. M. Escoffre, From concept to early clinical trials: 30 years of microbubble-based ultrasound-mediated drug delivery research, Advanced Drug Delivery Reviews (2024) 115199.
- [7] N. De Jong, R. Cornet, C. d. Lancée, Higher harmonics of vibrating gas-filled microspheres. part one: simulations, Ultrasonics 32 (6) (1994) 447–453.
- [8] C. C. Church, The effects of an elastic solid surface layer on the radial pulsations of gas bubbles, J. Acoust. Soc. Am. 97 (3) (1995) 1510–1521.
- [9] L. Hoff, Acoustic characterization of contrast agents for medical ultrasound imaging, Springer Science & Business Media, 2001.
- [10] P. Marmottant, S. van der Meer, M. Emmer, M. Versluis, N. de Jong, S. Hilgenfeldt, D. Lohse, A model for large amplitude oscillations of coated bubbles accounting for buckling and rupture, The Journal of the

- Acoustical Society of America 118 (6) (2005) 3499–3505. doi:10.1121/1.2109427.
- [11] A. A. Doinikov, P. A. Dayton, Maxwell rheological model for lipid-shelled ultrasound microbubble contrast agents, The Journal of the Acoustical Society of America 121 (6) (2007) 3331–3340.
- [12] S. Paul, A. Katiyar, K. Sarkar, D. Chatterjee, W. T. Shi, F. Forsberg, Material characterization of the encapsulation of an ultrasound contrast microbubble and its subharmonic response: Strain-softening interfacial elasticity model, The Journal of the Acoustical Society of America 127 (6) (2010) 3846–3857.
- [13] D. Chatterjee, K. Sarkar, A Newtonian rheological model for the interface of microbubble contrast agents, Ultrasound in medicine & biology 29 (12) (2003) 1749–1757.
- [14] K. Sarkar, W. T. Shi, D. Chatterjee, F. Forsberg, Characterization of ultrasound contrast microbubbles using in vitro experiments and viscous and viscoelastic interface models for encapsulation, The Journal of the Acoustical Society of America 118 (1) (2005) 539–550.
- [15] A. Katiyar, K. Sarkar, Excitation threshold for subharmonic generation from contrast microbubbles, The Journal of the Acoustical Society of America 130 (5) (2011) 3137–3147.
- [16] Q. Wang, K. Manmi, M. L. Calvisi, Numerical modeling of the 3D dynamics of ultrasound contrast agent microbubbles using the boundary integral method, Phys. Fluids 27 (2) (2015) 022104.
- [17] E. Johnsen, T. Colonius, Shock-induced collapse of a gas bubble in shockwave lithotripsy, J. Acoust. Soc. Am. 124 (2008) 2011—2020.
- [18] E. Johnsen, T. Colonius, Numerical simulations of non-spherical bubble collapse, J. Fluid Mech. 629 (2009) 231—-262.
- [19] Q. Wang, W. Liu, C. Corbett, W. R. Smith, Microbubble dynamics in a viscous compressible liquid subject to ultrasound, Phys. Fluids 34 (1) (2022).

- [20] S. J. Lind, T. N. Phillips, Spherical bubble collapse in viscoelastic fluids, J. Non-Newtonian Fluid Mech. 165 (2010) 56–64.
- [21] K. Foteinopoulou, M. Laso, Numerical simulation of bubble dynamics in a Phan-Thien-Tanner liquid: Nonlinear shape and size oscillatory response under periodic pressure, Ultrasonics 50 (2010) 758—-776.
- [22] S. J. Lind, T. N. Phillips, Bubble collapse in compressible fluids using a spectral element marker particle method. Part 2. Viscoelastic fluids, Int, J. Numer. Methods Fluids 71 (2013) 1103–1130.
- [23] C. Lang, M. Zhang, S. J. Schmidt, N. A. Adams, On spherical vapor bubble collapse in viscoelastic fluids, Applied Mathematical Modelling 123 (2023) 484–506.
- [24] H. Fogler, J. Goddard, Collapse of spherical cavities in viscoelastic fluids, Phys. Fluids 13 (5) (1970) 1135–1141.
- [25] J. Allen, R. Roy, Dynamics of gas bubbles in viscoelastic fluids. I. Linear viscoelasticity, J. Acoust. Soc. Am. 107 (2000) 3167–3178.
- [26] J. Allen, R. Roy, Dynamics of gas bubbles in viscoelastic fluids. I. Non-linear viscoelasticity, J. Acoust. Soc. Am. 108 (2000) 1640–1650.
- [27] D. Khismatullin, A. Nadim, Radial oscillations of encapsulated microbubbles in viscoelastic liquids, Phys. Fluids 14 (2002) 3534–3557.
- [28] X. Yang, C. Church, A model for the dynamics of gas bubbles in soft tissue, J. Acoust. Soc. Am. 118 (2005) 3595–3606.
- [29] E. A. Brujan, A first-order model for bubble dynamics in a compressible viscoelastic liquid, J. Non-Newtonian Fluid Mech. 84 (1999) 83–103.
- [30] E. A. Brujan, Cavitation bubble dynamics in non-Newtonian fluids, Polym. Eng. Sci. 49 (2009) 419–431.
- [31] W. Wu, Y. Liu, W. Smith, Q. Wang, Nonlinear three-dimensional modeling for encapsulated microbubble dynamics subject to ultrasound, Phys. Fluids 36 (9) (2024).

- [32] Z. Heidary, C.-D. Ohl, A. Mojra, Numerical analysis of ultrasound-mediated microbubble interactions in vascular systems: Effects on shear stress and vessel mechanics, Phys. Fluids 36 (8) (2024).
- [33] A. J. Szeri, B. D. Storey, A. Pearson, J. R. Blake, Heat and mass transfer during the violent collapse of nonspherical bubbles, Phys. Fluids 15 (2003) 2576–2586.
- [34] L. Rayleigh, On the pressure developed in a liquid during the collapse of a spherical cavity, Phil. Mag. 34 (1917) 94–98.
- [35] K. E. Morgan, J. S. Allen, P. A. Dayton, J. E. Chomas, A. L. Klibanov, K. E. Ferrara, Experimental and theoretical evaluation of microbubble behaviour: effect of transmitted phase and bubble size, IEEE Trans. Ultrason. Ferroelectr. Control 47 (6) (2000) 1494–1509.
- [36] J. B. A. F. Smeulders, C. Blom, J. Mellema, Linear viscoelastic study of lipid vesicle dispersions: Hard-sphere behavior and bilayer surface dynamics, Phys. Rev. A 42 (1990) 3483–3498.
- [37] R. E. Glazman, Effects of adsorbed films on gas bubble radial oscillations, J. Acoust. Soc. Am. 74 (3) (1983) 980–986.
- [38] C. E. Brennen, Cavitation and Bubble Dynamics, Oxford University Press, Oxford, 1995.
- [39] G. K. Batchelor, An Introduction to Fluid Dynamics, Cambridge University Press, London, 1967.
- [40] E. A. Brujan, The equation of bubble dynamics in a compressible linear viscoelastic liquid, J. Fluid Dyn. Res. 29 (2001) 287–294.
- [41] A. Pearson, J. R. Blake, S. R. Otto, Jets in bubbles, J. Eng. Math. 48 (2004) 391–412.
- [42] D. D. Joseph, Potential flow of viscous fluids: Historical notes, Int. J. Multiphase Flow 32 (2006) 285–310.
- [43] D. D. Joseph, Rise velocity of a spherical cap bubble, J. Fluid Mech. 488 (2003) 213–223.

- [44] S.-C. Georgescu, J.-L. Achard, E. Canot, Jet drops ejection in bursting gas bubble processes, Euro. J. Mech. B/Fluids 21 (2002) 265–280.
- [45] B. Rush, A. Nadim, The shape oscillations of a two-dimensional drop including viscous effects, Eng. Anal. Bound. Elem. 24 (2000) 43–51.
- [46] T. Funada, D. Joseph, Viscous potential flow analysis of Kelvin–Helmholtz instability in a channel, Journal of Fluid Mechanics 445 (2001) 263–283.
- [47] E. Canot, L. Davoust, Numerical simulation of the buoyancy-driven bouncing of a 2D bubble at a horizontal wall, Theor. Comput. Fluid Dyn. 17 (2003) 51–72.
- [48] D. Joseph, G. Beavers, T. Funada, Rayleigh–Taylor instability of viscoelastic drops at high Weber numbers, Journal of Fluid Mechanics 453 (2002) 109–132.
- [49] J. Blake, D. Gibson, Growth and collapse of a vapour cavity near a free surface, J. Fluid Mech. 111 (1981) 123–140.
- [50] J. Blake, B. Taib, G. Doherty, Transient cavities near boundaries. Part1. Rigid boundary, J. Fluid Mech. 170 (1986) 479–497.
- [51] J. R. Blake, D. C. Gibson, Cavitation bubbles near boundaries, Ann. Rev. Fluid Mech. 19 (1987) 99–123.
- [52] J. Best, The formation of toroidal bubbles upon the collapse of transient cavities, J. Fluid Mech. 251 (1993) 79–107.
- [53] Y. Tomita, P. Robinson, R. Tong, J. Blake, Growth and collapse of cavitation bubbles near a curved rigid boundary, J. Fluid Mech. 466 (2002) 259–283.
- [54] A. Pearson, E. Cox, J. Blake, S. Otto, Bubble interactions near a free surface, Eng. Anal. Bound. Elem. 28 (2004) 295–313.
- [55] S. J. Lind, T. N. Phillips, The influence of viscoelasticity on the collapse of cavitation bubbles near a rigid boundary, Theor. Comput. Fluid Dyn. 26 (1-4) (2012) 245–277.

- [56] S. Lind, T. Phillips, The effect of viscoelasticity on the dynamics of two gas bubbles near a rigid boundary, The IMA Journal of Applied Mathematics 77 (5) (2012) 652–677.
- [57] S. Lind, T. Phillips, The effect of viscoelasticity on the dynamics of gas bubbles near free surfaces, Physics of Fluids 25 (2) (2013).
- [58] M. J. Walters, An investigation into the effects of viscoelasticity on cavitation bubble dynamics with applications to biomedicine, Ph.D. thesis, Cardiff University (2015).
- [59] D. D. Joseph, T. Y. Liao, Potential flows of viscous and viscoelastic fluids, Journal of Fluid Mechanics 265 (1994) 1–23.
- [60] E. Brujan, C.-D. Ohl, W. Lauterborn, A. Philipp, Dynamics of laser-induced cavitation bubbles in polymer solutions, Acustica 82 (3) (1996) 423 430.
- [61] B. B. Taib, Boundary integral method applied to cavitation bubble dynamics, Ph.D. thesis, University of Wollongong (1985).
- [62] Q. Sun, E. Klaseboer, B. C. Khoo, D. Y. C. Chan, A robust and non-singular formulation of the boundary integral method for the potential problem, Eng. Anal. Bound. Elem. 43 (2014) 117–123.
- [63] M. J. Walters, T. N. Phillips, A non-singular boundary element method for modelling bubble dynamics in viscoelastic fluids., J. Non-Newtonian Fluid Mech. 235 (2016) 109–124.
- [64] Q. X. Wang, K. S. Yeo, B. C. Khoo, K. Y. Lam, Vortex ring modelling of toroidal bubbles, Theor. Comput. Fluid Dyn. 19 (2005) 303–317.
- [65] T. Rodrigues, R. Mota, L. Gales, L. Campo-Deaño, Understanding the complex rheology of human blood plasma, J. Rheol. 66 (4) (2022) 761– 774.
- [66] J. Wu, J. Pepe, W. Dewitt, Nonlinear behaviours of contrast agents relevant to diagnostic and therapeutic applications, Ultrasound Med. Biol. 29 (4) (2003) 555–562.
- [67] B. Y. Ni, A. M. Zhang, G. X. Wu, Numerical and experimental study of bubble impact on a solid wall, J. Fluid Eng. 137 (3) (2015) 1–16.

- [68] H. von Bibra, J. Voigt, M. Fröman, D. Bone, B. Wranne, A. Juhlin-Dannfeldt, Interaction of microbubbles with ultrasound, Echocardiography 16 (s1) (1999) 733–741.
- [69] B. Helfield, B. Y. Leung, X. Huo, D. Goertz, Scaling of the viscoelastic shell properties of phospholipid encapsulated microbubbles with ultrasound frequency, Ultrasonics 54 (6) (2014) 1419–1424.